Proceedings of

Workshop on Semiconductor Materials and Detectors,

November 19, 2013,
The University of Toledo, OH, USA

Jointly held by

Dr. Toru Aoki laboratory of Graduate School of Informatics, (Faculty of Informatics) at Shizuoka University

&

Nanotechnology and MEMS Laboratory of MIME Department at the University of Toledo

Edited by: Dr. Ahalapitiya H. Jayatissa of the University of Toledo and Dr. Toru Aoki of Shizuoka University

Introduction

This workshop will cover current research topics of Toru Aoki Laboratory at Shizuoka University and Nanotechnology and MEMS laboratory of MIME Department at the University of Toledo. The topics covered include electronic materials, nanomaterials, neutron and other radiation detectors. These materials have numerous applications in other fields such as, electronics, biotechnology, energy harvesting and sustainability of environments. The importance of semiconductor materials and device technology has been well documented by both industrial and academic communities worldwide. It is believed that breakthroughs in these fields will create more opportunities in safety aspects in nuclear power industries and security.

The workshop is intended to provide a exchange of ideas between two universities. Also, this activity support Japanese students to see US universities and research laboratories. The primary objectives of this workshop are to:

1) Facilitate interaction between students from Shizuoka University and the University of Toledo related to the fields of development and application of materials, with a special emphasis on sensors;
(2) Provide graduate students and undergraduate students with a forum to actively engage in research discussions, and professional development; and
(3) Create opportunities for the cultural exchange activities of both institutions.

This workshop will include one plenary speech on engineering ethics and contributed presentations. The plenary session has five presentations in the field of electronics materials, nonmaterial's, and characterization methods. These topics address timely and important issues around the globe.

The workshop provides opportunities for senior undergraduate students, graduate students and professors to actively engage in research discussions, and professional development. We hope participants will enjoy the technical program of this conference.

Program Schedule

November 19 (Tuesday),
Room # 4000 MIME Conference Room

9.30 am - 10.00 am	Introduction of Workshop Dr. A. H. Jayatissa and Dr. A. H. Aoki
Session Chair	Dr. A. H. Jayatissa
10.00 am - 10.30 am	Evaluation of Semiconductor Radiation Detector
10.30 am - 11.00 am	High-Contrast K-Edge CT by CdTe Photon Counting Detector
11.00 am - 11.30 am	Direction detection of radioisotope using a semiconductor radiation detector
11.30 am - 12.00 am	Low exposure CT using a photon counting detector
12.0 am - 1.00 am	Lunch Speech, Engineering Ethics Dr. Douglas Oliver, PhD, JD
Session Chair	Dr/ Toru Aoki
1.00 am - 1.30 pm	BGaN Semiconductor Neutron Detector
1.30 pm - 2.0 pm	Aqueous Hydrothermal Synthesis and Charaterization of Pyrite (FeS2) Nanoparticles
2.00 pm - 2.30 pm	Effects of Laser Irradiation on Optical, Structural and Gas Sensing Properties of Sputtered ZnO Thin Films
2.30 pm - 3.00 pm	Polypyrrole/Graphene Nanocomposite Synthesis and Conductivity Study
3.00 pm - 3.30 pm	Experimental Study on Thin Film Cu2ZnSnS4 Deposition by Spin Coating
3.30 pm - 4.00 pm	Estimation of thickness of ultra-thin materials by optical measurements
4.00 pm - 4.20 pm	Concluding Remarks: Dr. Toru Aoki Acknowledgements: Dr. A. H. Jayatissa

Table of Content

Evaluation of Semiconductor Radiation Detector

Hisaya Nakagawa[a], Hisashi Morii[b], Hidenoori Mimura[b] and Toru Aoki[b]

[a] Faculty of Informatics, Shizuoka University, Japan, cs10066@s.inf.shizuoka.ac.jp,
[b] Research Institute of electronics, Shizuoka University, Japan,

ABSTRACT:

In this study, we compared the characteristic of CdTe, CdZnTe and TlBr. In physical property and simulation, CdTe, CdZnTe, TlBr semiconductors have high detection efficiency for gamma-ray and X-ray. In current-voltage characteristic and capacitance-voltage characteristic, CdTe and CdZnTe semiconductors have schottky junction and TlBr has ohmic contact. In gamma-ray spectral measurement, the total absorption peak of CdTe is appeared sufficient. But that of CdZnTe and TlBr was not enough.

Key words: Semiconductor radiation detector, Thallium Bromide (TlBr), Cadmium Telluride (CdTe), Cadmium Zinc Telluride (CdZnTe)

I. Introduction

At present, the small X-ray tube and accelerator (about 1MeV) were developed and made practicable. The social infrastructure, containers which cannot be transmitted X-ray can become measured. However detectors have low sensitivity and low energy resolution.

We use CdTe semiconductor radiation detector. The thick CdTe is necessary to detect high energy. CdTe have weak point to increase leakage current when increase of thickness. We use CdZnTe which can inhibit leakage current even if it is thick. Also, detector which made heavy material to detect for high energy. We can use TlBr which is heavier than CdTe. In this study, we compared the characteristic of CdTe, CdZnTe, and TlBr with the aim of creating semiconductor radiation detector which has high sensitivity and high energy resolution for high energy at room temperature.

II. Physical property

Semiconductors used as semiconductor radiation detectors are Si or Ge. Si detector has low atomic number (14) and low density (2.33g/cm^3). Therefore, this is not suitable for the detection of high energy X-ray and gamma-ray. Ge detector has high atomic number (32) and high density (5.33g/cm^3). But, it low band gap energy (0.72eV) material. Therefore it has weak point that it is necessary to be cool. CdTe has high atomic number (Cd:48 Te:52), high density (5.85g/cm^3) and wide band gap energy (1.44eV). CdZnTe is crystal growth with Zn. Its average atomic number and density hardly change CdTe. However its band gap energy is slightly bigger than CdTe. TlBr has high atomic number (Tl:81 Br:35), high density (7.56g/cm^3) and wide band gap energy (2.68eV). In the semiconductor, the larger the atomic number and density are important for the high detection efficiency. And the wider band gap energy is for the less thermal noise. Table 1 shows physical property of semiconductor materials.

Table1
Physical property of semiconductor

	Density (g/cm^3)	Atomic Number	Band gap Energy (eV)
CdTe	5.85	48, 52	1.44
CdZnTe	5.81	48, 30, 52	1.6
TlBr	7.56	81, 35	2.68

III. Simulation

The simulation was performed by Electron Gamma Shower version 5 (EGS5) of High Energy Accelerator Research Organization. EGS5 is Monte Carlo particle transport calculation simulator. The size of all detectors was 10mm×10mm×0.5mm. And radiation source was ^{137}Cs source. Fig 1 shows the results of simulation. All detectors were shown 662keV the full energy peak. Therefore, they have high detection extraction for X-ray and gamma-ray in the simulation.

IV. Evaluation of electrical characteristic

Semiconductor is required charge transportation and extraction. In order to extract, there is a need as small as possible leakage current. And the size of depletion layer is also important. There are not included in the results of simulation. We researched

leakage current by current-voltage characteristic and depletion layer by capacitance-voltage characteristic.

IV-1. Current-voltage characteristic

Semiconductor which has ohmic contact follow ohmic law, when it was applied voltage. Semiconductor which has schottky junction starts to flow current above a certain voltage when it was applied forward current. When it was applied reverse bias, current flow very low in the ideal. But current flow it in actually. Current-voltage characteristic was measured by Semiconductor Parameter Analyzer (Hewlett Packard 4155B). Fig 2 shows current-voltage characteristic obtained from CdTe, CdZnTe and TlBr. Bias voltage applied from -100V to 100V at room temperature. In the TlBr's measurement, since the relationship between applied voltage and current is proportional connection, it has ohmic contact. The result of CdTe and CdZnTe, they have a schottky junction. And when they were applied reverse bias, the leakage current of CdTe is bigger than that of CdZnTe. Because the band gap energy of CdTe is narrower than that of CdZnTe.

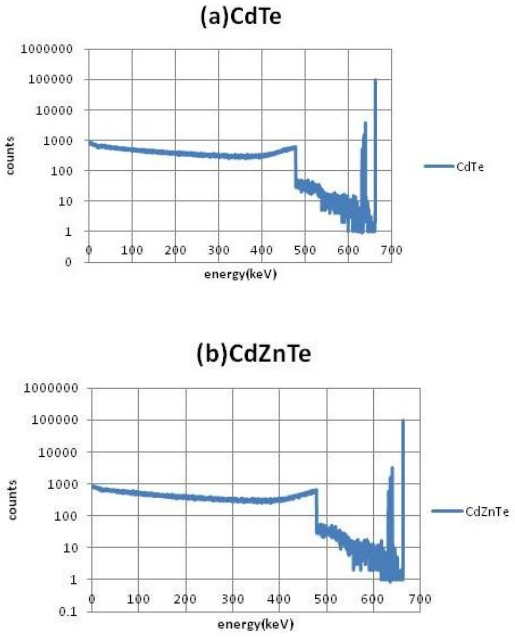

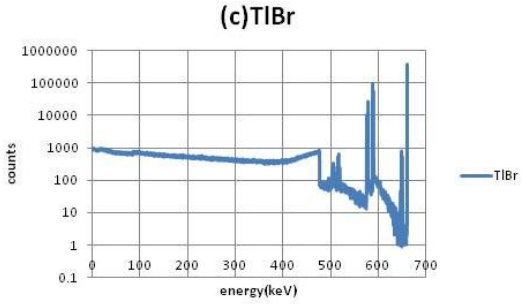

Fig.1 Simulation of the ^{137}Cs (a)Result of CdTe (b)Result of CdZnTe (c)Result of TlBr

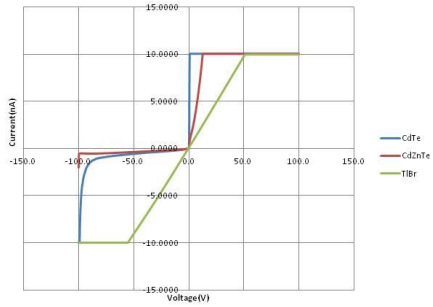

Fig.2 Current-voltage characteristic of CdTe, CdZnTe and TlBr

IV-2. Capacitance-voltage Characteristic

All detectors were performed capacitance-voltage characteristic to compare depletion layer spread when it was applied bias voltage. Capacitance-voltage characteristic was measured by Precision Impedance Analyzer (Agilent Technologies 4294A). Fig 3 shows capacitance-voltage characteristic obtained from CdTe, CdZnTe and TlBr. Bias voltage was applied from -40V to 40V at room temperature in dark room. In the result of this measurement, we cannot obtain results to discuss enough because of small capacity. But CdTe and CdZnTe semiconductors show dependent on voltage. TlBr semiconductor does not show dependent on voltage. Therefore, we can say CdTe and CdZnTe have schottky junction and TlBr has ohmic contact in conjunction with current-voltage characteristic.

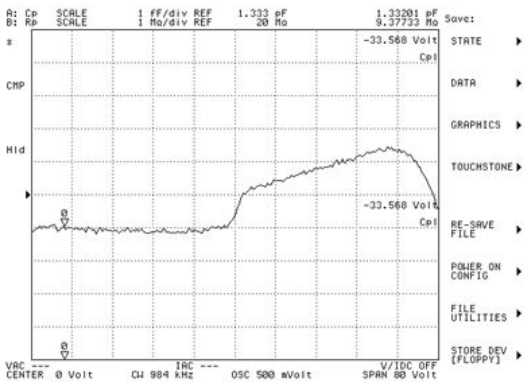

Fig3. Capacitance-voltage characteristic of CdTe

V. Gamma-ray spectral measurement

Gamma-ray energy of ^{137}Cs spectra was measured to evaluate the spectral characteristic of detections at the room temperature. The output signal from the amplifier were observed and recorded by multi-channel analyzer. When CdTe and CdZnTe were measured, bias voltage was applied 400V and shaping time was 0.5μs. When TlBr was measured, bias voltage was applied 100V and shaping time was 6.0μs. Fig 4 show gamma-ray spectral measurement obtained from CdTe, CdZnTe and TlBr. The full energy peak of CdTe is appeared sufficient. But that of CdZnTe was small, and that of TlBr was not appeared.

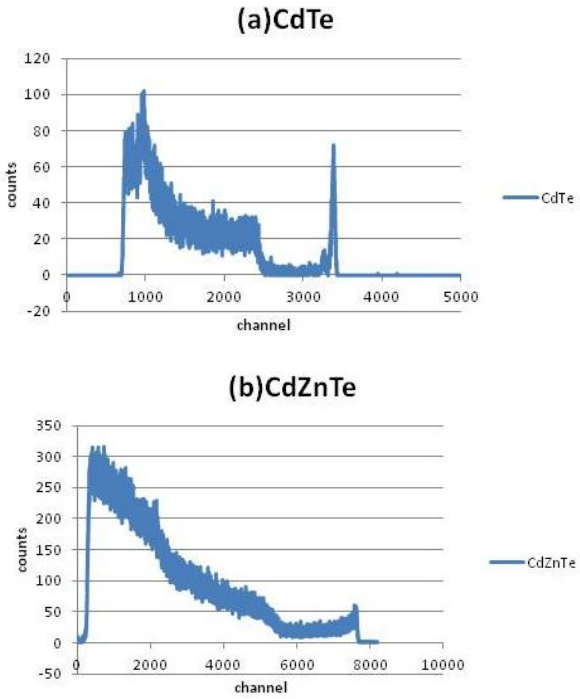

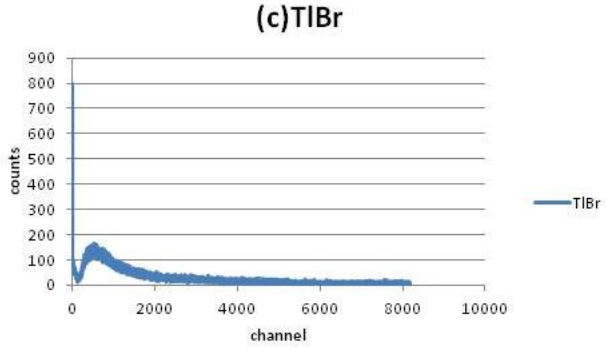

Fig 4. Gamma-ray spectral measurement of ^{137}Cs (a) Result of CdTe (b) Result of CdZnTe (c) Result of TlBr

VI. Conclution

In physical property and simulation, we found that detection efficiency of CdTe, CdZnTe, TlBr semiconductor for gamma-ray and X-ray is high. In current-voltage characteristic and capacitance-voltage characteristic, CdTe and CdZnTe semiconductor have schottky junction and TlBr has ohmic contact. And when CdTe and CdZnTe compared, the leakage current of CdZnTe is smaller than that of CdTe. In gamma-ray spectral measurement, the total absorption peak of CdTe was appeared sufficient. But that of CdZnTe was small, and that of TlBr was not appeared. In conclusion, three detectors was high detection efficiency in the theoretical value. However, the detectors were shown excellent results in the measured value. We think that these results are the problem which is crystalline.

References

[1] Tadayuki Takahashi , Kazuhiro Nakazawa CdTe/CdZnTe handotai wo mochiita gammasen kensyutuki to utyuu kannsokuhe no oyo (Application to space observation and gamma-ray detector)

[2] Fumihiko Hirose(2013) Handotai debaisu no yoten (Point of semiconductor device) http://fhirose.yz.yamagatau.ac.jp/(Accessed2013.11.01)

High-Contrast K-Edge CT by CdTe Photon Counting Detector

Kanichi. Ashitomi[1,2,*], Yukino. Imura[1], Hidenori. Mimura[1], Toru. Aoki[1,2]

[1]Research Institute of Electronics, Shizuoka University, Hamamatsu, Japan
[2]Graduate School of Informatics, Shizuoka University, Hamamatsu, Japan
3-5-1, Johoku, Naka-ku, Hamamatsu City, Shizuoka 432-8011, Japan
TEL&FAX: +81-53-478-1319
[*]e-mail: ashitomi@nvrc.rie.shizuoka.ac.jp

ABSTRACT:
X-ray are used in Medical treatment field as Roentgenogram, X-ray CT, PET and so on. It is potentially demanded for using low dose X-ray for human body. We conducted K-edge CT with photon-counting detector using cadmium telluride(CdTe) and made extracted images of Iodine which is used for contrast media at blood vessel in angiography. Though there are some noise on the others part as low dose X-ray, we can see blood vessel clearly. We can make higher contrast CT images of iodine by using high energy resolution.

Key words: low dose, k-edge, photon-counting, cadmium telluride

1. Introduction

Low dose X-ray imaging has been demanded on X-ray photography and X-ray computed tomography (X-ray CT), etc for medical care scene[1]. Angiography which uses contrast media is useful to see blood vessel clearly, though there is noise on the others part in low dose X-ray imaging. K-edge CT use feature of K-edge and information of X-ray energy for subtraction[2][3]. We can extract Iodine of blood vessel by K-edge CT and see it more clearly. We obtained information of X-ray energy by photon counting detector. We used information of X-ray energy for subtraction. We used CdTe semiconductor detector with high energy resolution. We discussed energy band width and over lapping energy band for K-edge CT. Energy band width and over 0lapping affect contrast of subtracted images. Two points above and below K-edge is the best of energy band width for K-edge CT. So, broad energy band width containing linear part of spectrum of X-ray and over lapping energy band makes low contrast because it is low for difference of amount of X-ray counts for two CT images. Then, we try to use strict band width for K-edge CT. As CdTe semiconductor detector has high energy resolution, we can use strict X-ray energy band width for K-edge CT. Using narrower energy band width for K-edge CT makes higher contrast.

2. K-Edge CT

We carried out K-edge radiography using iodine-based contrast media. The iodine contrast media(30mg/ml) put into a hole in an acrylic vessel and it was measured by X-ray CT with the CdTe detector using photon counting method(X-ray tube voltage:150kV, current 8uA). K-edge energy is a specific property of X-ray energy of each material. The X-ray attenuation coefficient for a material has discontinuous relation below and above K-edge energy. K-edge of iodine is 33.2keV. Since the X-ray attenuation coefficient for bones and muscles don't have K-edge at 33.2keV, we can see large difference of image of iodine in two CT images used data below and above K-edge without bones and muscles image. Then, we extracted iodine image by subtraction of these two CT images.

Our detector has high energy resolution(~1keV). Therefore, we found out the optimum width for the highest contrast of iodine CT image. In the result, the contrast ratio of this photon counting CT system is

1:11(acryl : iodine). The contrast ratio of estimated system which has low energy resolution(~16keV) is 1:4. Our system improves the contrast ratio of subtraction of iodine CT image.

3. Experiment

We carried out X-ray CT and got information of X-ray energy. Fig.2 shows an illustration of the experiment system. X-ray tube voltage is 150kV. X-ray tube current is 8uA. X-ray detector is CdTe detector (X-123, amptek)

4. Result and Discussion

We can see large difference of image of iodine in two CT images(bandwidth 4keV)(fig.3) used data below(low energy) and above(high energy) K-edge. Fig.4 shows profiles of both two CT images. Red line is for profile of CT image used high energy band, blue line is for low energy band. CT values of part of Iodine are difference between two CT image. Then, we extracted iodine image by subtraction of these two CT images(fig.5).

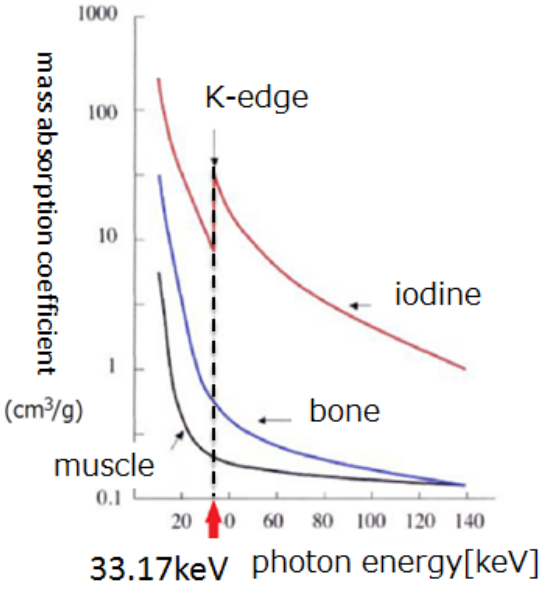

Fig.1 : Mass absorption coefficient of iodine, bone and muscle[4]

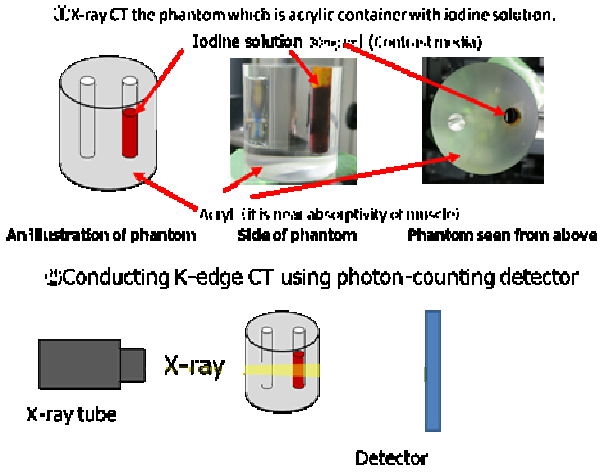

Fig.2 : The experiment system

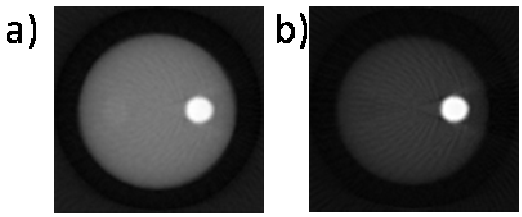

Fig.3 : CT images of a) below and b) above K-edge energy of I

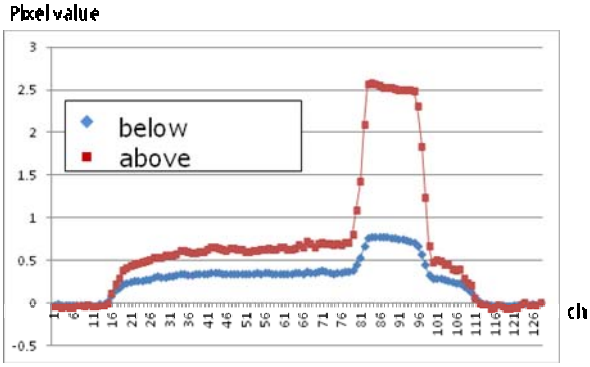

Fig.4 : Profiles of CT images of below and above K-edge

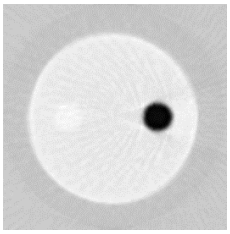

Fig.5 : The image of the subtraction of both CT image

Fig.6 shows result and comparison of subtraction images of three previous methods. Previous method A : Using overlapped X-ray energy data for subtraction. It is assumed to use two X-ray tubes. Previous method B : Using X-ray energy data beyond K-edge for subtraction. It is assumed to use low

resolution detector. Method C : Proposed method. Using X-ray data which is cut strictly for subtraction.

Fig.7 shows profiles of three methods. The graph shows proposed method C and method B is higher contrast than method A at part of Iodine. Pixel value at part of acryl of Method C is nearer 0 than method B. This indicates part of acryl of subtracted image by method C is disappeared and we can see only part of Iodine.

Fig.8 is variation of subtracted images by using some energy bandwidth. Part of acryl of image is disappeared further as getting narrower and narrower the energy band width for subtraction. And, we can see the part of Iodine more clearly. Fig.9 shows that using narrower energy band for subtraction makes higher contrast. Pixel value of part of acryl is nearer 0 that is pixel value of air. Pixel value of part of Iodine is farther from 0. Fig.10 shows that the narrower energy band width we use for subtraction, the nearer 0 pixel value of part of acryl and - Fig.11 shows – the farther pixel value of part of Iodine from 0 which is the pixel value of air.

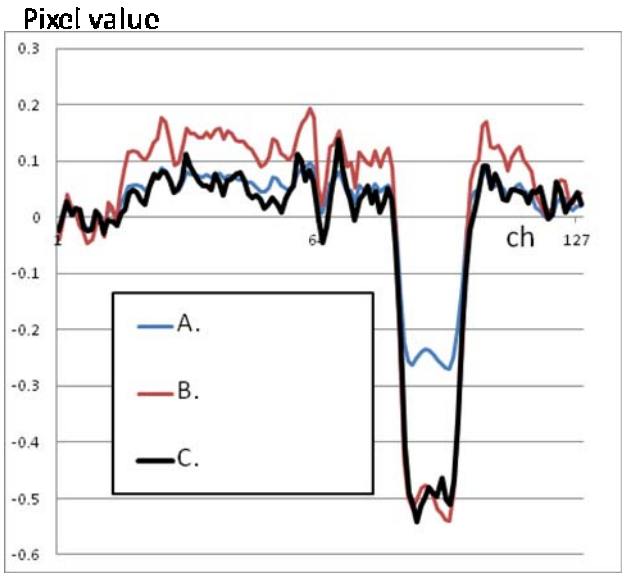

Fig.7 : Profiles of A(Previous method 1), B(Previous method 2) and C(Proposed method)

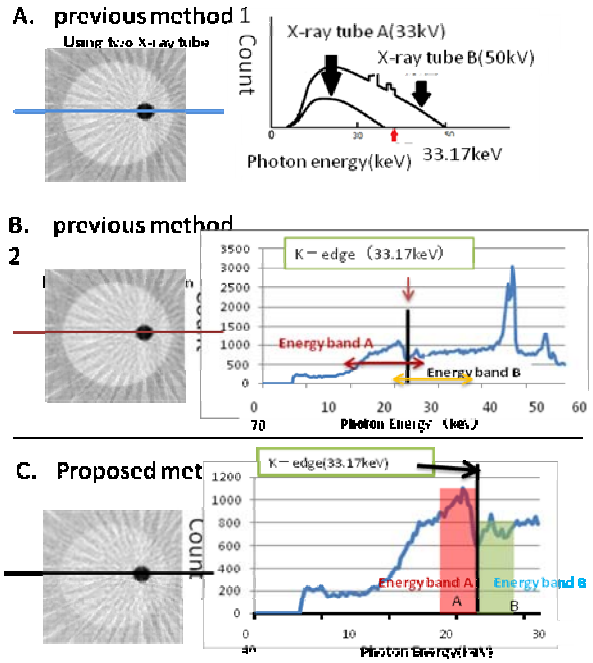

Fig.6 : Comparison of three methods

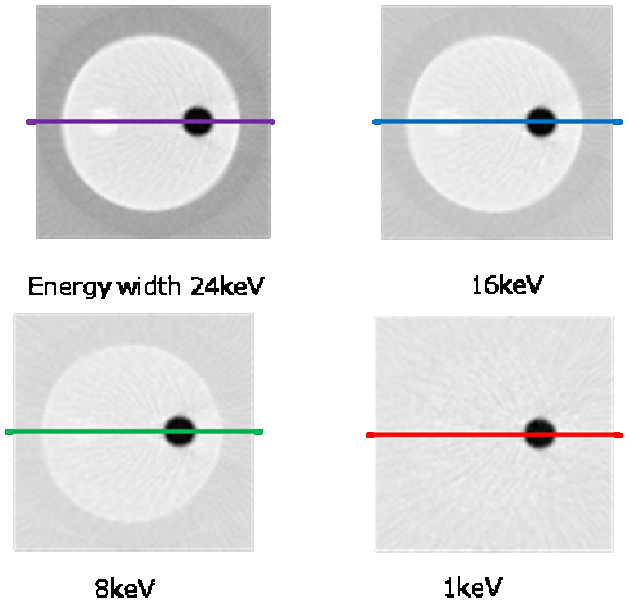

Fig.8 : Variation of subtracted image by using some energy bandwidth

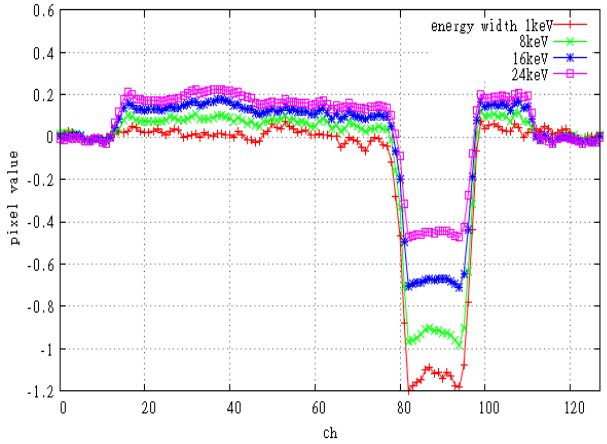

Fig.9 : Profiles of four images

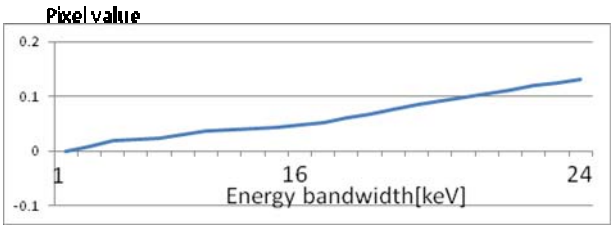

Fig.10 : Pixel value at part of acryl

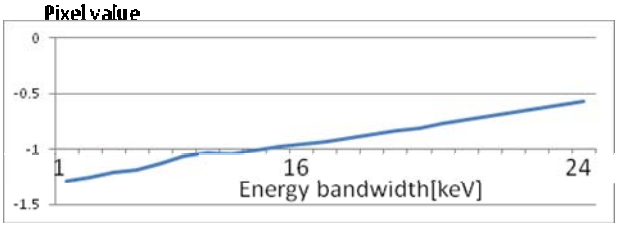

Fig.11 : Pixel value at part of Iodine

5. Conclusion

We discussed effects of using energy band width and over lapping data of X-ray for K-edge CT.

Using narrower energy band width for K-edge CT is higher contrast.

Using strict energy band data for K-edge CT makes higher contrast than over lapping data.

Acknowledgments: This work was supported by grants from Keiryo Research
Foundation, Promotion and Mutual Aid Corporation for
Private Schools of Japan, Japan Science and Technology
Agency (JST), New Energy and Industrial Technology

Reference

[1] Ryo Matsushita, Eiichi Sato, Yutaka Yanbe, Hiraku Chiba, Tomoko Maeda, Osahiko Hagiwara, Hiroshi Matsukiyo, Akihiro Osawa, Toshiyuki Enomoto, Manabu Watanabe,Shinya Kusachi, Shigehiro Sato, Akira Ogawa, and Jun Onagawa, "Low-Dose-Rate Computed Tomography System Utilizing 25 mm/s-Scan Silicon X-ray Diode and Its Application to Iodine K-Edge Imaging Using Filtered Bremsstrahlung Photons", JJAP-52-042202 (2013).
[2] Manabu Watanabe, Eiichi Sato, Purkhet Abderyim, Hiroshi Matsukiyo, Akihiro Osawa, Toshiyuki Enomoto, Jiro Nagao, Seiichiro Nomiya, Keitaro Hitom e, Akira Ogawa, Shigehiro Sato, Toshio Ichimaru, " Energy-discriminating K-edge x-ray computed tomography system", Proc. of SPIE Vol. 7080 70800B-5(2008).
[3] Eiichi Sato, Purkhe Abderyim, Hiroshi Matsukiyo, Akihiro Osawa, Toshiyuki Enomoto, Manabu Watanabe, Jiro Nagao, Seichiro Nomiya, Keitaro Hitom, Akira Ogawa, Shigehiro Sato, Toshio Ichimaru, "Energy-discriminating x-ray camera utilizing a cadmium telluride detector", Proc. of SPIE Vol. 7079 70790Z-5(2008).
[4]"denno nyumon sho", http://www.mb.ccnw.ne.jp/sfujii/satuei/satuei06.html

BGaN Semiconductor Neutron Detector

Masaki Nakamura[a,] Katsuhiro Atsumi[b,] and Takayuki Nakano[b]
Hidenori Mimura[c], Toru Aoki[a ,c]

[a] Faculty of Informatics, Shizuoka University, Japan, cs10069@s.inf.shizuoka.ac.jp,
[b] Faculty of Engineering, Shizuoka University, Japan,
[c] Research Institute of Electronics, Shizuoka University, Japan,

ABSTRACT:
This paper proposes novel neutron detector used by BGaN semiconductor. The principle of this detector is detection the α-ray due to GaN that is released as a result of nuclear reactions that arising catching neutron by boron. We showed creating α-ray detector and neutron has detected by BGaN.

Key words: Semiconductor, Boron, Gallium Nitride (GaN), Boron Gallium Nitride (BGaN)

1. Introduction

There is demand on various occasions the neutron detector, for example, security sector, medical sector, and industrial sector, and so on. The neutron detectors that are currently mainly used are ^{3}He neutron detector and scintillator neutron detector. There are advantages and disadvantages to each of these detectors. The ^{3}He neutron detector has an advantage that high sensitivity for neutron and can be separated the neutron and γ-ray. However, disadvantage of ^{3}He is fewer. The Scintillator neutron detector has quick response, but there is a drawback difficult to separate the neutron and γ-ray. Therefore we tried to develop a detector with a performance like redeeming of the two detectors. Namely our goal is development high sensitivity detector for neutron with low sensitivity for γ-ray instead of ^{3}He detector.

2. Materials

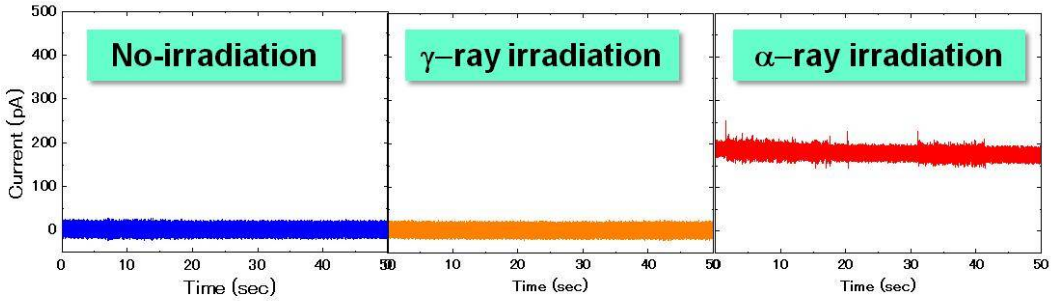

Fig. 2 The output current of GaN was measured with α-ray and/or γ-ray

First, the material that we have focused was boron. As shown Figure 1, boron can capture neutron than almost materials. However, neutrons do not have electric charge and boron has no charge transportation characteristics. We considered that trying to utilize α-ray that caused by the (n, α) reaction when boron caught a neutron. If the α-ray is detected by semiconductor, we can confirm the detection of neutron indirectly. The semiconductor have focused was GaN. The major reason for choosing a GaN semiconductor is its high carrier transportation properties proven as a blue LED. In addition, GaN has a good factor of low sensitivity of γ-ray. We aim to create a neutron detector that is possible to achieve the goal using BGaN combines boron converter and GaN semiconductor.

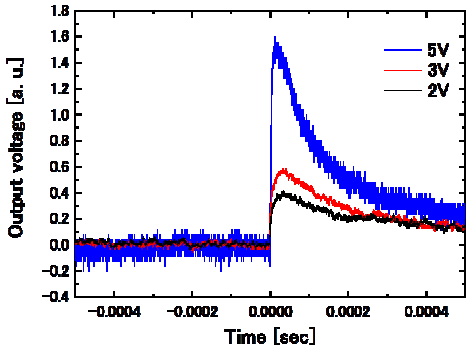

Fig. 3 The detected signal of a neutron by BGaN detector

3. Experiments

We conducted on experiments whether detect the neutron based on this principle. One is related to GaN, we have to the performance of high sensitivity of α-ray, low sensitivity of γ-ray. The experimental method is irradiated to GaN with α-ray and γ-ray, to ascertain the current amount severally. As a radiation

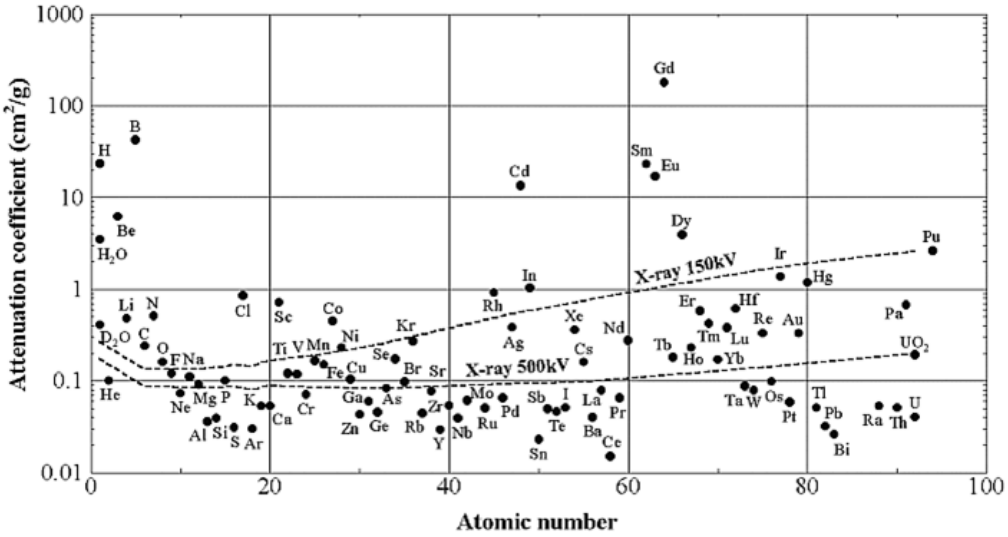

Fig. 1 Thermal neutron and X-ray mass attenuation coefficients for the elements

source, we use ^{241}Am. For BGaN, we have to ascertain it can detect the neutron. The experimental method is irradiated to BGaN with neutron, to ascertain whether currents flowing. We use ^{252}Cf as neutron source.

4. Results and Discussion

Figure 2 shows the experimental results on GaN. From this figure, the current was almost unchanged compared no irradiation with γ-ray irradiation. The current when irradiated with α-ray is increased significantly compared with no irradiation. From these results, GaN is low sensitivity for γ-ray and high sensitivity for α-ray. Figure 3 shows the experimental result on BGaN. This figure shows that neutrons could be detected by suggested mechanism.

5. Conclusion

We studied the neutron detector using a semiconductor. Boron and GaN is proposed as converter, and as base material. Experimental results were shown that GaN can be detected to separate the α-ray and γ-ray and BGaN can be detected neutron. The suggested neutron detection mechanism is realized using BGaN. We would like to improve this detector hereafter.

Low exposure CT using a photon counting detector

Ryudai Hatanaka, Kanichi Ashitomi, Yukino Imura, Hidenori Mimura, Toru Aoki

Faculty of Informatics, Research Institute of Electronics, Shizuoka University,
3-5-1 Jouhoku, Naka-ku, Hamamatsu, Shizuoka 432-8011, Japan
hatanaka@nvrc.rie.shizuoka.ac.jp

ABSTRACT:
In order to evaluate the performance of photon counting detector, we get CT scan image the acrylic phantom as an object in practice. From the experimental results, we found that clear image is obtained by increasing the number of steps than the scan time, and also found that amount of exposure is reduced considerably compared to conventional detector.

Key words: 4 keywords can be given. All letters are lower case. word files only. PDF files cannot be accepted.

1. INTRODUCTION

The Computer Tomography(CT) is essential in modern medical field. The advantage of CT is there are many, such as clear image represented by the CT value, reduction of inspection time, and so on. On the other hand, the patient is inevitable exposure to some extent in order to determine that the material exactly, make a image quality improvement. For this reason, one of the challenges is that of how to achieve a CT of low exposure in any way.

In this paper, we rated the performance of the photon counting detector is expected to be one way to achieve low radiation CT.

The advantage of using a photon counting detector are varied. One of the advantage, after scanning CT image, we can calculate the required parts by selecting the energy band. If you scan at least once, It is possible to determine the substance by checking the energy band. Therefore, we do not have to scan many times. In addition, the detector can measure the X-ray photons by converting directly to

charge, this is also one of the advantages. For this reason, the image quality and the energy resolution is improved. As a result, it is possible to reduce the irradiation dose.

Object of this experiment is to evaluate the performance of the photon counting detector in order to compare the performance of a conventional detector.

We used the Cadmium Telluride(CdTe) semiconductor detectors as a photon counting detector. CdTe is substance absorption and radiation detection efficiency is high. Also, it is a substance there is no aging.

II. **Experimental Methodology**

In order to evaluate the performance of the detector, we got CT scan in practice.

We used acrylic phantom as an object, X-ray tube(x-ray150: Hamamatsu Photonics) and a detector(X-123 CdTe type radiation detector) in the CT scan.

We arranged to be a straight line in the order of X-ray tube, an object and a detector.

At this time, the X-ray tube and the object, the object and the detector were placed so that distance of them is 40cm straight line (Figure 1). And, when the subject was placed on a rotating stage is rotated 360 degrees, we were measured two cases of step 36 or 72 the rotation step. Further, we have cases divided into three types of 0.1, 0.25, 0.5 seconds each scan time per step.

We used acrylic phantom as an object, X-ray absorption rate of the phantom is similar to that of the human body. We filled with water and an aqueous iodine solution of 30g / L as a contrast agent, respectively, two holes that are open to the phantom. Specification for the phantom is shown in Figure 2.

Voltage and current of the X-ray tube was set 150kV, 8μA respectively.

In this paper, amount of exposure is represented by "current of the X-ray tube (mA) × total irradiation time (s)". Thus, amount of exposure is "0.008 × (scan time per step × number of steps)".

After the experiment, I confirmed amount of exposure and contrast of the CT value, which is the quality of the image.

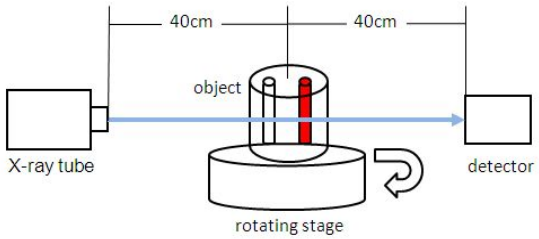

Fig. 1 Arrangement plan

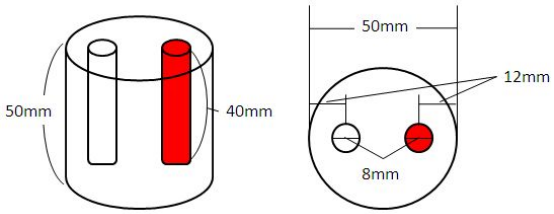

Fig. 2 Specification of phantom

III. Result and Discussion

CT image of the result was shown in Figure 3 and 4.

And we showed the image profile which was expressed as CT values the dotted line of the CT image in Figure 5 and 6.

(Note, in the part of the 0.5 second and 72 steps which is an image of figure 4, artifact of the streak can be seen for the deficiencies. But please ignored because it is not the intention in this experiment.)

When we compare the CT images of the results of each, we found that the larger the number of steps, the more artifacts are reduced. In particular, it can be seen that the noise is reduced when compare the results of the image profile which is shown in Figures 5 and 6. Further, the contrast of the iodine portion is larger in the case of 72 steps.

For the CT scan time, there was no change that affects the image quality significantly in any number of steps.

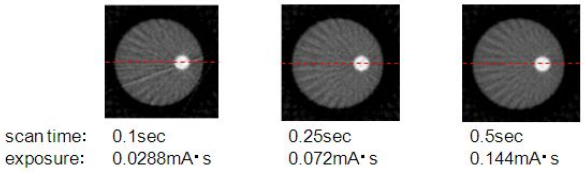

Fig. 3 Scan results in the case of 36 steps

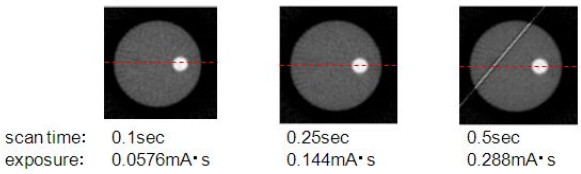

Fig. 4 Scan results in the case of 72 steps

Amount of exposure when using a conventional detector is 500 ~ 1000mA・s approximately, Thus we found that is suppressed exposure appreciable in the results of Figure 3 and 4. But, the image in the case of 72 steps, It is not the crisp image quality enough for use as a medical, Therefore, it is necessary to increase the image quality to the same extent as conventional detector by increasing the number of steps further. On the other hand, about the CT scan time, since there has been no change in image quality in 0.5 seconds is the longest and 0.1 seconds is the shortest, it was found that it can be scanned in a short time more.

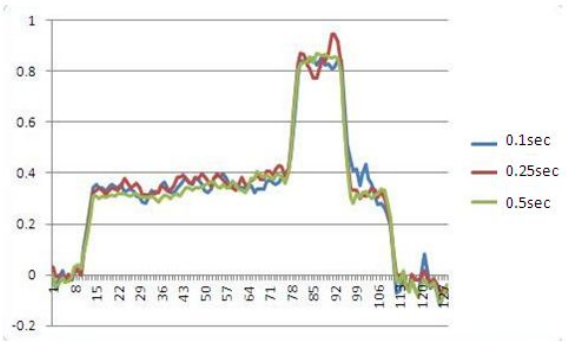

Fig. 5 Image profile in the case of 36 steps

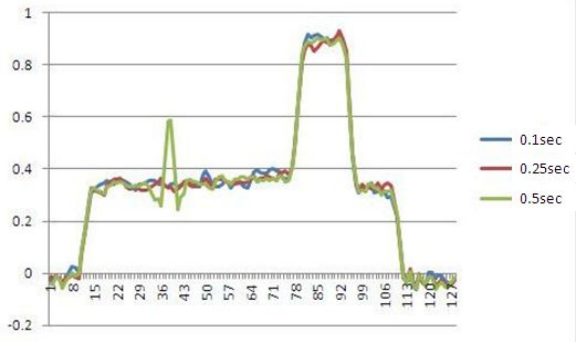

Fig. 6 Image profile in the case of 72 steps

IV. Conclusions

In the future, we will adjust the image quality by setting more number of steps and short scan time. Then, we're going to scan to be the image quality that is adjusted in both detectors and to compare the exposure of both.

In the end, we want to achieve low exposure CT by indicating the superiority of the photon counting detector performance from this comparison.

V. References

[1] Diagnostic imaging article collection|Social care corporation Daiyukai|Official site (gazoushindan kijishu | shakaiiryouhojin daiyukai | koushikisaito). 22 Sept. 2013. <http://www.daiyukai.or.jp/recruit/article/index.php>

[2] X-ray CT (X-ray computed tomography) - ATOMICA -. 22 Sept. 2013. <http://www.rist.or.jp/atomica/data/dat_detail.php?Title_Key=08-02-01-02>

[3] B [28]What do you see in the image examination of the brain?| | Brain |Cardiovascular this and that|National Cardiovascular Information Service ([28］nou no gazoukensa de nani ga wakaru?). 22 Sept. 2013. <http://www.ncvc.go.jp/cvdinfo/pamphlet/brain/pamph28.html>

[4] About X-ray, ultrasound, CT, MRI(rentogen,tyouonpa,CT,MRI ni tuite). 22 Sept. 2013. <http://www002.upp.so-net.ne.jp/andouiin/kennsa.html>

[5] MCA infarct with CT perfusion | Image | Radiopaedia.org. 22 Sept. 2013. <http://radiopaedia.org/images/889549>

[6] What is CdTe - acrorad(CdTe toha - acrorad). 22 Sept. 2013. <http://www.acrorad.co.jp/cdte.html>

Direction detection of radioisotope using a semiconductor radiation detector

Takuto Sanada[a] , Toru Aoki[a,b] , Hidenori Mimura[b], and Hisashi Morii[c]

[a] Faculty of Informatics, Shizuoka University, Japan, cs10049@s.inf.shizuoka.ac.jp,
[b] Research Institute of Electronics, Shizuoka University, Japan,
[c] ANSeeN, Japan

ABSTRACT:

In Fukushima of Japan, a large amount of radiation material was released outside of the nuclear power plant by the earthquake occurred in March 2011, and effect on crops and people are concerned. On the other hand, radiation is not visible, decontamination work is rough going. Therefore we did locating of the radioisotope using the directional dependence of the CdTe detector with high energy resolution. The experimental results showed a difference in sensitivity due to the incident direction of radiation, but not sufficient, we found to be necessary to devise to improve the dependence.

1. Introduction

Tokyo Electric Power Company Fukushima Daiichi nuclear power plant was severely damaged by the Tohoku-pacific ocean earthquake and tsunami occurred in 2011 and fell into a serious situation that release a large amount of radioactive material to the exterior of the plant. In order to remove the radioactive material, a hard decontamination work is being continued even today. Since the wide range is contaminated and conventional radiation detector does not have the ability to identify the location of the radioactive material, to detect points of high doses called "hot spots" is not easy. Therefore in order to improve the efficiency of the decontamination work, we propose the development of hot spots detection system using the directional dependence of semiconductor detectors with high energy resolution.

2. Prior research

On the relationship between the half-life, cesium is particularly concerned the long term effect in the radioactive materials released in an accident at the Fukushima Daiichi nuclear power plant. Gamma camera is an apparatus for performing position location of a substance that emits γ-rays as cesium. There are mainly two types of gamma camera.

2.1. Compton camera

Compton camera is a device that utilizes the Compton scattering, which is one of the interaction of the substance with γ-rays and consists of absorption material for causing the photoelectric absorption and scattering material for causing the Compton scattering. It use the information of scattering, absorption position and the scattering angle calculated from the scattered energy to locate the γ-ray source, then project it on the image taken by camera to visualize the position of the radioactive material. This device is efficiency because it uses individual γ-ray entered the detector and it is also excellent in removing the background by forming an image by focusing the energy range. System is complex to analyze vast number of data of channels. Therefore the camera was large and costly immediately after the earthquake, but they are improving in recent years.

2.2. Pinhole type

The gamma camera based on this method, the shielding material surrounding the detector functions as a collimator and background subtraction. In order to identify the position of γ-rays source from the positional relationship between the window and the detector that has absorbed γ-rays, the incident γ-rays are limited to those that go straight to the window from the radioactive material. This device needs heavy shielding material such as lead to prevent γ-ray from being incident except those passed the window. Therefore this camera is too heavy to carry for decontamination workers.

3. Theory

In this study, we are taking advantage of the characteristics of the radiation detector that sensitivity varies with the angle of incidence of the radiation and attempt to develop a system for performing position location of radioactive isotope. Semiconductor detector has higher energy resolution than other solid detector, so we selected it.

3.1. γ-ray detection with semiconductor detector

Through the reaction of the detector, γ-rays can be raised to the conduction band the number of electrons according to their energy. Since the detector is a semiconductor diode, it is possible to measure the energy deposition and the number of γ-ray reacted at the detector inside by detecting current flowing due to the incident radiation with high reverse bias. Semiconductor detectors with Ge and Si have been commercialized mainly, however we use CdTe detector that has high effective atomic number and can also be operated at room temperature.

3.2. Incident directional dependence

Distance the radiation passes through crystal before leaving it depends sensitively on the shape of the crystal, location of the incident, and angle of incidence. In addition, the effective area of the detector for receiving the incident radiation varies with the angle of incidence. For performing measurements targeting γ-ray source, it is necessary to consider the effect of the interaction of the substance with γ-rays, i.e. photoelectric effect, compton scattering, electron pair production. However, γ-ray emitted from 137Cs doesn't cause electron pair production because it does not exceed the threshold value of electron pair production. So, we can't expect to take advantage of this reaction. Photoelectric effct is just absorption reaction, however compton scattering, which can change the direction of travel of the photon clearly affects the sensitivity of the detector. Angle differential cross-section of Compton scattering is given by the formula of Klein-Nishina.

$$\frac{d\sigma}{d\Sigma} = \frac{1}{2} r^2 \frac{1}{\{1+\alpha\}^2} \left\{ 1 + \cos^2\theta + \frac{\alpha^2}{1+\alpha} \right\} \qquad (1)$$

$$\alpha = \frac{h\nu}{m_0 c^2}(1 - \cos\theta)$$

Where hv is the energy of photon, $m_0 c^2$ is rest mass of the electron, and r is the classical radius of the electron. We have applied the equation (1) with respect to photons that the energy is 662KeV, and show the relationship between the differential scattering cross-section and photons scattered per unit solid angle at Fig. 1.

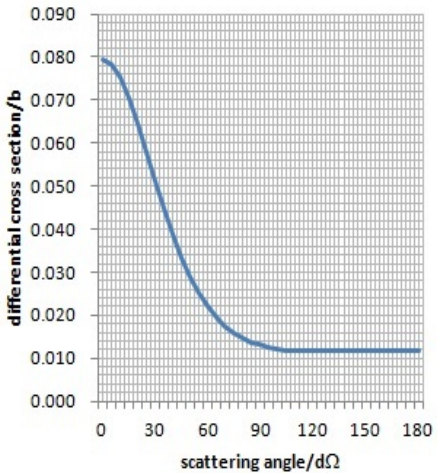

Fig.1 Differential cross section of photn

In this energy, most of Compton scattering is a forward scattering that scattering angle is less than 90 degrees. Practically, it must be taken into account the influence of Doppler broadening effects due to the momentum of the electrons in atoms, and multiple scattering in the crystal. In parallel with the experiment, we perform a simulation using the electron and photon transport calculation code jointly developed by the University of Michigan, Stanford University, and the High Energy Accelerator Research and Development Organization to reveal the effect of the interaction of photons and atoms give the directional dependence.

4. Experiment

We measured the 137Cs using Schottky CdTe detector (manufactured by Acrorad Co.Ltd.). The detector holds titanium and indium electrode on the anode and platinum electrode on the cathode and the size of detector is 10×10×0.5mm. Electrical signal from the detector was amplified by pre-amplifier (type 5102, manufactured by CLEAR-PULSE). We measured 137Cs installed at the distance of 20cm from the detector. The detector was reverse-biased for 500 V, and the measurement time was 70 minutes. The detector was fixed on the stage and is controlled within 0.01 degrees by stage controller. Measurements were performed in each case incident angle was 0 degrees, 30 degrees, 45 degrees, 60 degrees, and 90 degrees with the detector surface.

5. Results and discussion

Fig. 2 is an energy spectrum of the each angle of incidence, and comparison of the spectrum was performed in order to clarify the differences between each angle. Gross of the total absorption peak(662KeV) showed a maximum value, 8877, and a minimum value, 7361, at 60 and 90 degrees, respectively. Detection efficiency of the total absorption reaction to the total number of detected was maximum at 60 degrees. Peaks of the 200KeV peaks and 33KeV was confirmed that the count is decreased as the incident angle is gradually increased from 0 degrees. On the other hand, there was little difference by incident angle in compton scattering section.

Maximum detection efficiency was observed when the angle of incidence was 60 degrees, probably because it was optimum conditions in this experiment with respect to the effective area of the detector and the distance γ-ray passes through. Difference of Compton scattering was hardly observed, we must devise methods for increasing the dependency. The peak of 200KeV is observed only in the case of measuring 137Cs with CdTe detector and well reflects the incident angle.

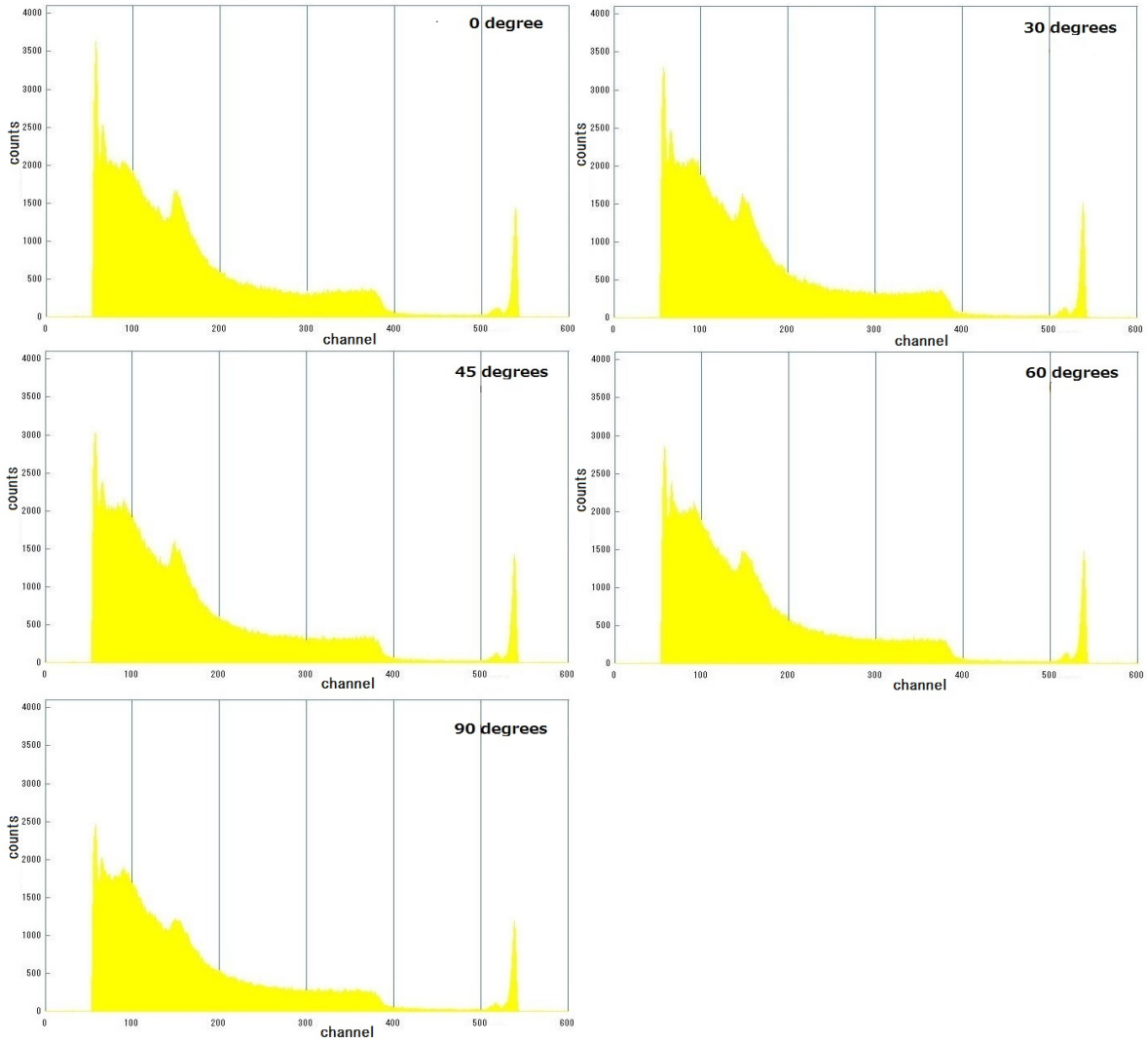

Fig.2 Energy spectrum of each angle

However, this peak has unknown cause of generation and is not reproduced in the simulation. Therefore we must clarify the cause to utilize the peak.

6. Summary

Obtained directional dependence was not enough in this experiment, then we plan to use the collimator and compton scattering material in addition to the CdTe detector to improve directional dependence. On the other hand, we will also plant to check the experimental data and the theoretical value obtained by simulation.

References

[1] Tadayuki Takahashi, Shinichirou Takeda, Shin Watanabe, Visualization of diffusion situation of radiation material by Compton camera, Journal of the Physical Society of Japan Vol.68, 2013, pp382-386

Aqueous Hydrothermal Synthesis and Charaterization of Pyrite (FeS_2) Nanoparticles

Zhengqi Shi and Ahalapitiya.H.Jayatissa

Nanotechnology and MEMS Laboratory, Department of Mechanical, Industrial, and Manufacturing Engineering, University of Toledo, Toledo, OH 43606, USA, Corresponding Author: ajayati@utnet.utoledo.edu

ABSTRACT:

FeS_2 nano-particles was successfully synthesized by a simple, low-temperature aqueous hydrothermal reaction and annealed in 450 ^oC for 30 min. The microstructure and electrical properties were determined. The X-ray diffraction (XRD) pattern indicated pure pyrite phase of the annealed powder and a small average grain size of 29.47 nm. The Scanning Electron Microscope (SEM) study displayed a larger grain size at same magnitude and indicated higher crystal growth rate than thermal sulfuration approach. Resistance dependence on temperature was studied and the result follows Arrhenius equation with a small activation energy (29.27 meV) and small resistance of the powder ($\sim 10^1\ \Omega$)

Key words: pyrite; hydrothermal; characterization

1. INTRODUCTION

Pyrite (FeS_2) was separated widely and known as one of the most common mineral[1]. Its composition are also among most abundant elements on earth. Pyrite has a cubic FCC crystal structure like NaCl: the S_2^{2-} were located as Cl^- while Fe^{2+} stay at positions for Na^+. However, another possible structure for FeS_2 is marcasite. The difference is the arrangement of S_2^{2-} around iron ions[2]. Due to the high absorption coefficient ($\sim 10^5$ cm^{-1}, two magnitude higher than Si)[3] and similar band gap energy (0.95 eV) as poly-silicon (1.1 eV), FeS_2 is considered as an alternative candidate for thin film solar cell application[4].

Various synthesis approaches for pyrite powders and thin films have been developed including metal-organic chemical vapor deposition (MOCVD)[5-8], thin-film thermal sulfuration of pre-deposited films[9-12], electro-deposition[13] and solution-based methods[14-19]. For MOCVD, thermal sulfuration and electrodeposition, those relative costly process were usually multi-steps including thermal annealing under sulfur atmosphere to obtain enough S atoms for pyrite FeS_2. Moreover, those two approaches indicated the pyrite phase may be stable only above 450^{o}C since almost all FeS_2 films were treated never below 450^{o}C in conventional synthesis[5]. The solution-based approaches could serve as cost-effective process but most of the reaction were accomplished under high temperature or long reaction periods[14,18]. In addition, some works were done even with hazardous solvents[16,17]. Those facts limited the development of solution-based approach.

In this work, an simple, low-temperature aqueous hydrothermal approach is applied to synthesize pure phase pyrite. A short annealing at 450^{o}C was followed to investigate the .approximate crystal growth. The reaction conditions required to synthesize iron pyrite nano-particles, microstructure and electrical properties of the FeS_2 powders were all discussed.

II. Experimental

A hydrothermal approach was applied for the synthesis of iron pyrite nano-particles. In a typical approach, 5 mmol Ferrous Sulfate Crystal ($FeSO_4{\cdot}7H_2O$, certified ACS, Fisher Scientific), 20 mmol Ammonium Thiosulfate ($(NH_4)_2S_2O_3$, 99%, Alfa Aesar) were separately dissolved completely with DI water. Then these two solutions were mixed together and sonicated for 15 min. After the sonication, the total solution was sent into the aluminum pressure cooker (model No.921, Wisconsin aluminum foundry). This pressure cooker was filled with DI water up to 1/4 of its total capacity. After the preheating at 550^{o}C for 1h, the internal pressure reached the designed 15 psi. Then the hydrothermal reaction started and continued for 9h at 500^{o}C. The dark precipitate was later retrieved by filtration and washed with DI water for 5 times and ethanol for 1 time. To observe the crystal growth, the room-temp dried precipitate was annealed in nitrogen at 450^{o}C for 30 min.

An X-ray diffractometer (PANalytical X'Pert Pro MPD) with Cu Kα radiation was applied to indicate the crystal structure of FeS_2 powder. The scanning range was from $2\theta=20^o$--70^o with $\lambda=1.5418$ Å. To investigate the surface morphology, a vacuum deposition on clean glass substrate was applied. The surface morphology of the as-deposited FeS_2 thin film was then observed with a scanning electron microscopy (SEM, JEOL 6100). In order to test the electrical properties of FeS_2 powder, small amount of powder (1 mm thickness) was sealed in a glass tube (7.9 mm internal diameter) with its two ends fixed tightly with graphite electrodes. The tube was buried in oil and the whole system was heated on hotplate in air. The electrode was connected to an electronic resistance meter (Keithley 2420 model) to collect the resistance response between 25^{o}C and 140^{o}C

III. Results and Discussion

The black powders after short annealing under 450^{o}C, 30 min was characterized by powder X-ray Diffraction. The relative pattern was shown in Fig.1. After comparison with JCPDS 01-071-1680, the peaks are clearly referred to a pure cubic pyrite structure and match with the reference in both the peak position and ratio of intensity. Relative planes for all peaks are labeled in Fig.1 and the most dominant peak indicated (200) planes. However, since (113) and (102) also own high intensity peaks,

it's hard to justify the preferential growth direction of this iron pyrite powder.

In order to estimate the average grain size of this annealed powder, Scherrer equation shown below was applied with β as the full width of half maximum of the first several high intensive peaks and k is a constant of 0.9:

$$\tau = \frac{k\lambda}{\beta \cos\theta}$$

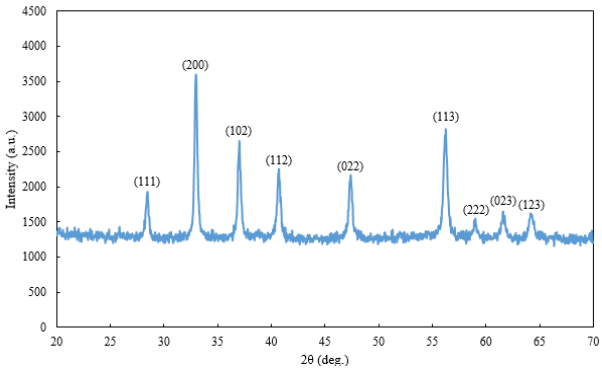

Fig.1 X-ray Diffraction Patterns of annealed FeS_2 particles

The corresponding calculation was shown in Table.1 below. The results indicated an average grain size of 29.47 nm. To verify this calculation, a SEM measurement was applied to analyze the grain size and microstructure of this annealed iron pyrite nano-particles. Fig.2 indicated a small and uniformly distributed FeS_2 particles. The average grain size could be roughly observed approximately as 50 nm, which demonstrated the previous estimation was not accurate enough. Moreover, a highly crystal growth rate of the iron pyrite can be estimated after comparison with long-time annealing from L.Meng et al[10]. This could be another advantage of hydrothermal synthesis. Also, the particles are mostly close-packed and very few holes could be observed. However, some unexpected large particles also occur in Fig.2 (lighter, larger patterns). This is inferred as tungsten sulfide since tungsten boat was applied in the thermal vacuum film deposition. Few particles of WS_2 may formed during deposition and finally occur in the final thin film.

Table.1 Calculation of average grain size of annealed FeS_2 powder, data in lower right corner was the average of the three grain sizes above.

2θ (deg.)	FWHM (deg.)	Planes (hkl)	Grain Size (nm)
32.99	0.26	(200)	31.99
37.10	0.28	(102)	29.93
56.20	0.34	(113)	26.49
			29.47

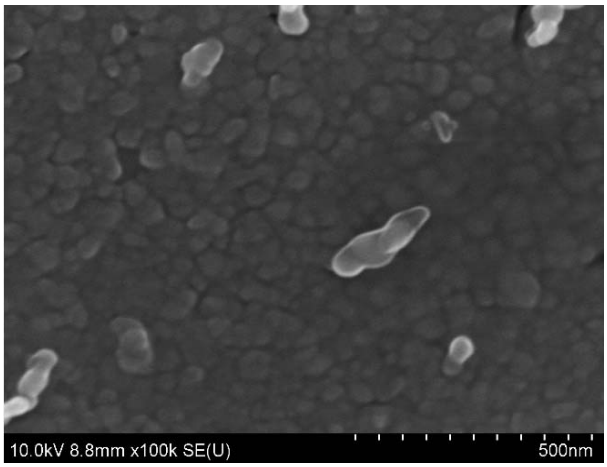

Fig.2 SEM morphology of the annealed FeS_2

Fig.3 shows the relationship of logarithm on reciprocal of resistivity to the reciprocal of temperature. The result indicates this annealed FeS_2 nano-particles has a semiconductor behavior. This dependence was linearly fitted and the fitting curve could be described via Arrhenius equation:

$$\sigma = \sigma_0 \exp(-\frac{\Delta E_o}{kT})$$

where σ, k, T means conductivity, Boltzmann constant and temperature, respectively. During the measurement, the oil temperature was between room temperature (25°C) and 140°C. From the result, the activation energy of the annealed FeS_2 powder can be calculated and the value was 29.27 meV, which matches well with N.Berry et al.[8] (31 meV and 29 meV) shown as the inserted plot in Fig.3. Moreover, the small resistance of FeS_2 powder (~10^1 Ω) indicated great conductivity of this material.

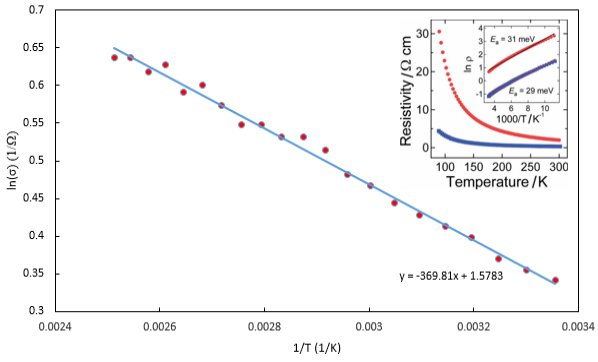

Fig.3 Arrhenius plot of resistance versus temperature. Insert plot shows the similar plot from N.Berry et al[8]

IV. Conclusions

Pyrite nano-particles was synthesized via one-step aqueous hydrothermal approach. The XRD pattern indicates a single pure pyrite phase after short annealing under 450°C for 30 min. No preferential growth direction was observed. The grain size was estimated via Scherrer equation from three major peaks and the result was 29.47 nm. However, further SEM morphology observation resulted in a higher average grain size around 50 nm, which indicated a higher crystal growth rate than thermal sulfuration on iron thin film. Resistivity dependence on temperature was measured and the result follows the Arrhenius equation. The resistance of FeS_2 powder was around several ohm scale. The activation energy was calculated as 29.27 meV.

Acknowledgments:

This work was supported by a grant (ECS-0928440) from the National Science Foundation (NSF) of USA.

References

[1] Eun Jung Kim, Bill Batchelor, Synthesis and characterization of pyrite (FeS_2) using microwave irradiation, Materials Research Bulletin 44 (2009) 1553-1558.
[2]I.Uhlig, R.Szargan, H.W.Nesbitt, K.Laajalehto, Surface States and Reactivity of Pyrite and Marcasite, Applied Surface Science 179 (2001) 222-229.
[3]A.Ennaoui, S.Fiechter, C.Pettenkofer, N.Alonso-Vante, K.Bilker, M.Bronold, C.H6pfner, H.Tributsch, Iron Disulfide for Solar Energy Conversion, Solar Energy Materials and Solar Cells 29 (1993) 289-370.
[4]Wadia, Cyrus; Wu, Yue; Gul, Sheraz; Volkman, Steven; Guo, Jinghua; Alivisatos, A. Paul, Surfactant-Assisted Hydrothermal Synthesis of Single phase Pyrite FeS2 Nanocrystals, Chemistry of Materials 2009, 21, 2568-2570.
[5]A.Ennaoui, S.Fiechter, W. Jaegermann, H.Tributch, Photoelectrochemistry of Highly Quantum Efficient Single ‐Crystalline n ‐ FeS2 (Pyrite), Journal of Electrochemical Society, 1986 volume 133, issue 1, 97-106.
[6]Ben Meester, Liesbeth Reijnen, Albert Goossens, Joop Schoonman, Synthesis of Pyrite (FeS2) Thin Films by Low-Pressure MOCVD, Chem. Vap. Deposition 2000, 6, No. 3.
[7]J.Oertel, K. Ellmer, W. Bohne, J. Röhrich, H. Tributsch, Growth of n-type polycrystalline pyrite (FeS2) films by metalorganic chemical vapour deposition and their electrical characterization, Journal of Crystal Growth 198/199 (1999) 1205-1210.
[8]Nicholas Berry, Ming Cheng, Craig L. Perkins, Moritz Limpinsel, John C. Hemminger, Matt Law, Atmospheric-Pressure Chemical Vapor Deposition of Iron Pyrite Thin Films, Advanced Energy Materials 2012, 2, 1124–1135.
[9]C.de las Heras, I.J.Ferrer, C.Sánchez, Pyrite thin films: Improvements in their optical and electrical properties by annealing at different temperatures in a sulfur atmosphere, Journal of Applied Physics. 74(7), 1 Oct. 1993.
[10] L.Meng, Y.H.Liu, L.Tian, Structural, optical and electrical properties of polycrystalline pyrite (FeS_2) films obtained by thermal sulfuration of iron films, Journal of Crystal Growth 253 (2003) 530-538.
[11]N.Hamdadou, A.Khelil, J.C.Bernède, Pyrite FeS_2 films obtained by sulphuration of iron pre-deposited films, Materials Chemistry and Physics 78 (2003) 591-601.
[12]R.J.Soukup, P.Prabukanthan, N.J.Ianno, A.Sarkar, C.A.Kamler, D.G.Sekora, Formation of pyrite (FeS_2) thin films by thermal sulfurization of dc magnetron sputtered iron, Journal of Vacuum Science and Technology A 29(1), Jan/Feb 2011.
[13]Youzhong Dong , Yufeng Zheng, Xiaogang Zhang, He Duan, Yanfei Sun, Yanhua Chen, FeS2 (pyrite) electro-deposition thin films and study of growth mechanism, Science in China Ser. E Engineering and Materials Science 2005 Vol.48 No.6 601611 601.
[14]D. Wei, K. Osseo-Asare, Aqueous synthesis of finely divided pyrite particles, Colloids and Surfaces A: Physicochemical and Engineering Aspects Volume 121, Issue 1, 10 March 1997, Pages 27−36.
[15]S.Kar, S.K.Mandal, D.Das, S.Chaudhuri, Wet chemical synthesis of iron pyrite and characterization by Mössbauer spectroscopy, Materials Letters 58 (2004) 2886-2889.
[16]J.Puthussery, S.Seefeld, N.Barry, M.Gibbs, M.Law, Colloidal Iron Pyrite (FeS_2) Nanocrystal Inks for Thin-Film Photovoltaics, Journal of the American Chemical Society. 2011, 133, 716-719.
[17]Su-Ching Hsiao, Chih-Ming Hsu, Szu-Ying Chen, Yu-Hsun Perng, Yu-Lun Chueh, Lih-Juann Chen, Lih-Hsin Chou, Facile synthesis and characterization of high temperature phase FeS2 pyrite nanocrystals, Materials Letters Volume 75, 15 May 2012, Pages 152−154.
[18]A. Moradi Golsheikh, N.M.Huang, H.N.Lim, C.H.Chia, I. Harrison, M.R.Muhamad, One-pot hydrothermal synthesis and characterization of FeS2 (pyrite)/graphene nanocomposite, Chemical Engineering Journal Volume 218, 15 February 2013, Pages 276−284.
[19]Xiaoqing Qiu, Min Liu, Toru Hayashi, Masahiro Miyauchi, Kazuhito Hashimoto, Solution-based synthesis of pyrite films with enhanced photocurrent generation, Chem. Commun., 2013, 49, 1232-1234.

Effects of Laser Irradiation on Optical, Structural and Gas Sensing Properties of Sputtered ZnO Thin Films

Yue Hou and Ahalapitiya H. Jayatissa*

Nanotechnology and MEMS Laboratory, Mechanical, Industrial and Manufacturing Engineering (MIME) Department, The University of Toledo, OH 43606, USA.
*Corresponding author: Ahalapatiya H. Jayatissa
E-Mail: ajayati@utnet.utoledo.edu

ABSTRACT

The effect of laser irradiation on the optical, structural and gas sensing properties of Al-doped ZnO thin films with different laser power was investigated. Al-doped ZnO thin films were deposited by rf magnetron sputtering on glass substrate. The Al-doped ZnO thin film exhibits higher optical transparency in the visible region after laser irradiation treatment. At the same time, the laser irradiation results in a broadening of optical band gap. All the Al-doped ZnO thin films show a c-axis preferred orientation. The peak intensity decreased with high laser power irradiation. The grain size of Al-doped ZnO thin films continuously decreased with increasing laser power. The gas sensing behavior was investigated for H_2 under different concentrations in air. The results indicate that the sensor characteristics such as sensing response, response and recovery time can be significantly improved by optimizing the laser power.

Key words: Al-doped ZnO, rf magnetron sputtering, laser irradiation, gas sensor

1. INTRODUCTION

Zinc oxide (ZnO) a well-known semiconducting material and has attracted a great deal of attention due to its versatile properties and large application potentials. ZnO has been used in many applications such as surface acoustic wave devices (SAW), thin film transistors, varistors and gas sensors [1-4]. Undoped ZnO generally possesses high resistance which is a barrier for energy saving. Impurity doping is an effective way to achieve high conductivity of ZnO. ZnO can be doped with a wide variety of impurity ions such as Al, Sn, Mn and Sb. Among them, Al as one of the group III elements with an ionic radius of 0.072 nm is one of the best candidate. Many researchers have reported the high conductivity of Al-doped ZnO (AZO) [5,6]. In recent years, laser irradiation has emerged as a novel heat treatment method due to its local and rapid thermal heating ability. Compared with convention furnace heating, laser beam heats a small local area rather than the whole system. Therefore, it is worthwhile to investigate the effect of laser irradiation on the thin film properties. In this study, the rf magnetron sputtered AZO thin films were irradiated by a pulsed laser with a wavelength of 532 nm under different laser power. The influences of laser irradiation on the optical, electrical and gas sensing properties of AZO thin films were investigated as a function of laser power.

2. EXPERIMENTS

Al-doped ZnO films were deposited on glass substrates by an rf magnetron sputtering system using a metallic AZO (2wt% Al_2O_3, 98wt% ZnO) target with 99.9% purity of 50.8 mm diameter and 6.35 mm thick. The target to the substrate distance was 40 mm and was kept fixed. The vacuum chamber was first evacuated to 2 x 10^{-6} Torr using a cryopump. The magnetron sputtering was carried out in a mixture of oxygen and argon (99.999%, O_2/Ar: 1/1) by supplying rf power at a frequency of 13.56 MHz and the rf power was 100 W. The introduced high-purity gas mixture raised the pressure in the chamber and deposition pressure was around 5.3 x 10^{-3} Torr. The films were deposited for 10 min without heating the substrate. Before the deposition, the target was pre-sputtered for a few minutes to remove the possible contamination on the surface. The films were deposited on alkali free glass substrates. The glass substrate was first rinsed thoroughly with detergent and then washed completely with deionized water and acetone to remove the dust particles and organic residuals. After the deposition, the as-deposited films were annealed in a tube furnace at 550^{o}C for 3 h in the air.

The laser irradiation was carried out by a pulsed laser system (Quantronix Osprey-532-5-0) with a wavelength of 532 nm. The deposited sample was divided into three pieces and two of which were subjected to laser irradiation with different laser power. The laser beam diameter was about 80 μm, and the incident laser power was varied from 268 to 735 mW. The as-deposited films, laser-irradiated films with 268 mW and laser-irradiated films with 735 mW were designated as sample-1, sample-2 and sample-3, respectively.

In this study, the microstructure was investigated by X-ray diffraction (PANalytical X'Pert Pro MPD) using Cu Kα radiation source. The scanning range was from $2\theta = 25^o$ to 45^o with $\lambda = 1.5418$ Å. The average grain size D was estimated based on Scherrer equation, which is given by $D = K\lambda/(\beta\cos\theta)$, where K is a constant, β is the full width at the half maximum (FWHM) of the XRD peak. The optical transmittance was investigated in the wavelength range of 300 – 1000 nm using an UV/Vis spectrophotometer (SHIMADZU UV-1650PC). The gas sensing behavior was tested in a homemade device. The configuration of the system was given in our previous paper [7]. Finger-patterned Au electrodes were developed on the sample surface by optical lithography. The samples were mounted in the glass chamber. The operating temperature was constantly monitored by a thermocouple. Different concentrations of target gases were introduced into the chamber with 100 ccm constant airflow.

3. RESULTS AND DISCUSSIONS

3. 1 OPTICAL PROPERTIES

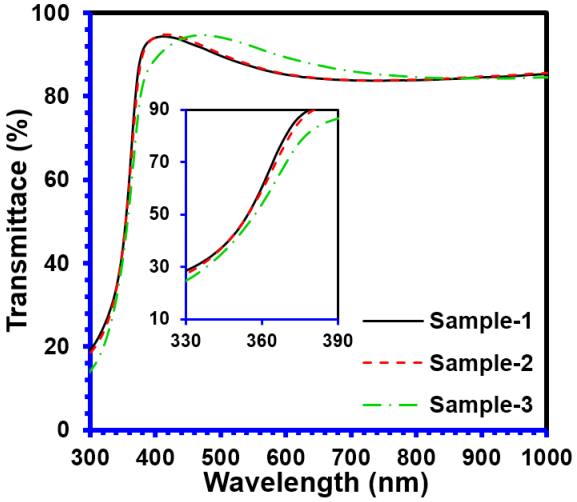

Fig. 1. Optical transmittance spectra of AZO thin films.

Figure 1 shows the optical transmittance spectra of as-deposited and laser-irradiated AZO thin films. All the thin films exhibited an average transmission of higher than 85% in the visible region with a very sharp fundamental absorption edge. The high transparency implies that all the thin films have good structural homogeneity and crystallinity. It is seen that sample-2 showed slightly higher transparency than that of sample-1. The transparency increased with further increase of the laser power to 735 mW (sample-3). The inset of Fig. 1 shows the transmittance in the wavelength range of 330 to 390 nm. A shift of absorption threshold was observed. This feature indicated the shrinkage of optical bandgap. This phenomenon may be attributed to both the stress relaxed and the increase of oxygen vacancies or interstitial ZnO atoms during laser irradiation treatment [8].

3. 2 Structural properties

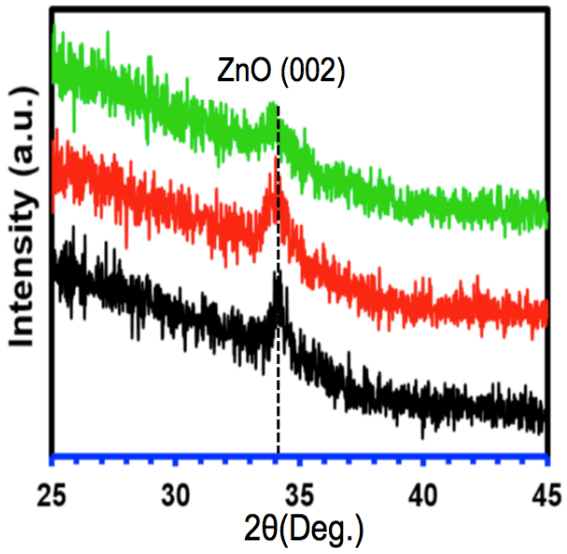

Fig. 2 X-ray diffraction pattern of AZO thin films.

Figure 2 shows the X-ray diffraction pattern of as-deposited and laser-irradiated AZO thin films in the range of $2\theta = 25^{o}$ to 45^{o}. Only one prominent peak was observed at round $2\theta = 34.4^{o}$ corresponding to the (002) plane. It indicated that the films had a preferential orientation along the c-axis normal to the substrate surface. The phenomenon may be attributed to the nature of the grains that it tends to grow along the lowest surface energy plane. It is also observed that the (002) peak of sample-2 became strong and broad compared to that of sample-1. However, the (002) peak deteriorated with further increase of laser power. Table 1 shows the FWHMs, position and average grains of (002) peak for as-deposited and laser-irradiated AZO thin films. It is seen that the laser irradiation broadened the peak and increased the FWHM values as increasing laser power. According to Table 1, the average grain size decreased from 13.17 to 6.68 nm with increasing laser power from 0 to 735 mW.

TABLE I
THE FWHMS, POSITION AND AVERAGE GRAIN SIZE FOR AS-DEPOSITED AND LASER-IRRADIATED AZO THIN FILMS.

Sample #	FWHM (Deg.)	Position (Deg.)	Average grain size (nm)
Sample-1	0.66	34.13	13.17
Sample-2	1.09	34.04	8.97
Sample-3	1.3	33.93	6.68

3. 3 GAS SENSING BEHAVIOR

The gas sensing behavior of as-deposited and laser-irradiated AZO thin films were examined at an operating temperature of 135°C. Various concentrations of H_2 were introduced into the chamber. The gas response S of gas sensor was defined as $S = [(R_a - R_g)x100\%]/R_a$, where R_a is the resistance of the sensor in air and R_g is the resistance of the sensor in H_2-air mixture gas.

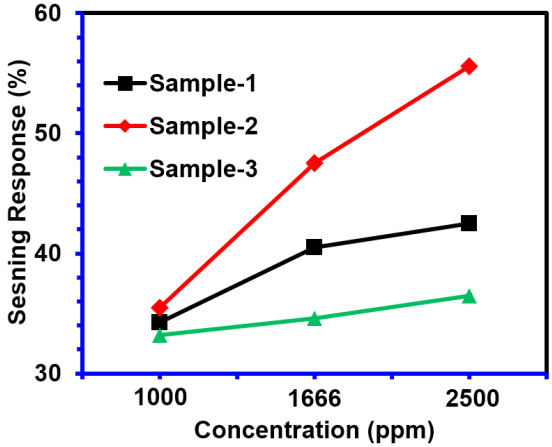

Fig. 3 Variation of sensing response as a function of H_2 concentration for AZO sensors.

Figure 3 shows the dependence of sensing response versus H_2 concentration ranging from 1000 to 2500 ppm for all the AZO sensors. It is seen that the sensing response increased with the increase of H_2 concentration. The sensing response of sample-2 increased significant compared with that of sample-1. However, sample-3 showed a decrease in sensing response compared with that of sample-1. The result indicates that the sensing response of sputtered AZO sensors enhanced by laser irradiation with optimum laser power. Further increase of laser power over the optimum power level resulted in a decrease in sensing response.

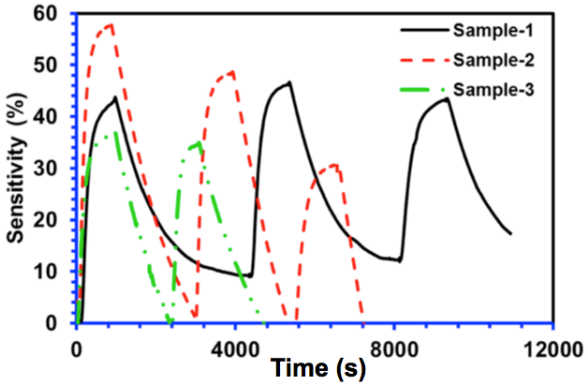

Fig. 4. Dynamic response and recovery of AZO sensors.

Figure 4 shows the response and recovery characteristics of all the AZO sensors. It is seen that all the AZO sensors responded immediately to H_2 as it introduced into the chamber. All the sensors reached 70% of its saturation sensing response in tens of seconds and saturated in minutes. It is worthwhile to notice that the as-deposited AZO sensor (sample-1) did not recovery to the original baseline after exposing to H_2. However, all the laser-irradiated AZO sensors recovered to the original baseline. Moreover, the laser-irradiated AZO sensors (sample-2 and 3) showed much shorter recovery time than that of as-deposited AZO sensors (sample-1).

4. Conclusions

Al-doped ZnO thin films deposited by rf magnetron sputtering have been post treated by laser irradiation with different laser power. The optical, structural and gas sensing behavior of laser-irradiated ZnO thin films were investigated as a function of laser power. The optical transparency increased after laser irradiation. The absorption edge continuously shifted with increasing laser power. The XRD peaks broadened after laser irradiation. The grain size of the AZO thin film decreased as the increase of laser power. The gas sensor performance indicated that the sensing response was improved significantly with optimum laser power. Furthermore, the response and recovery time shortened after laser irradiation treatment.

Acknowledgment: This research was supported by grants (Grant number: 0933069 and 0928440) from National Science Foundation (NSF), USA.

References

[1] V.K. Varadan, V.V. Varadan, H. Subramanian, Sens. Actuators A 90 (2001) 7–19.
[2] T. Soga (Ed.), Nanostructured Materials for Solar Energy Conversion (2006) Amsterdam.
[3] U. Ozgur, Y.I. Alivov, C. Liu, A. Teke, M.A. Reshchikov, S. Dogan, V. Avrutin, S.J. Choand, H. Morkoc, Journal of Applied Physics 98 (2005) 041301.
[4] D.L. DeVoe, Sens. Actuators A 88 (2001) 263–272.
[5] K. Lin, Y. Chen, K. Chou, Solution derived Al-doped zinc oxide films: doping effect, microstructure and electrical property, J Sol-Gel Sci Technol 49 (2009) 238-242.
[6] H. Zhou, D. Yi, Z. Yu, L. Xiao, J. Li, Preparation of aluminum doped zinc oxide films and the study of their microstructure, electrical and optical properties, Thin Solid Films 515 (2007) 6909-6914.
[7] Y. Hou, A.M. Soleimanpour, A.H. Jayatissa, Low resistive aluminum doped nanocrystalline zinc oxide for reducing gas sensor application via sol–gel process, Sensor Actuat. B-Chem. 177 (2013) 761-769.

[8] R. Hong, C. Wei, H. Bo, Z. Fan, J. Shao, Influence of CO2 laser irradiation on the structure and photoluminescence of zinc oxide thin films, Thin Solid Films 485 (2005) 262-266.

Polypyrrole/Graphene Nanocomposite Synthesis and Conductivity Study

Weiling Wang and Ahalapitiya H. Jayattisa[a]

Nanotechnology and MEMS Laboratory
Mechanical, Industrial, and Manufacturing Engineering Department
The University of Toledo, OH 43607, USA

[a]Corresponding author. Email Address: ajayati@utnet.utoledo.edu.

ABSTRACT:

A conductive nanocomposite consists of polypyrrole and graphene was formed by one step in-situ polymerization. The mixture of graphene isopropanol dispersion and pyrrole monomers was doped with hydrochloride, and oxidized by ammonia pursulfate (APS). A black liquid ink was obtained after centrifuging and dividing the resultant, which was brush-deposited on glass slides to form a nanocomposite film. XRD was used to characterize the composition of this nanocomposite. The electron transport mechanism of this nanocomposite was studied. The temperature dependence of conductivity could be described by Arrhenius equation. Graphene fillers was found to contribute to conductivity negatively because it causes the increase in disorder. O_2 plasma treatment was conducted and found to have the potential to reduce activation energy.

Key words: polypyrrole, graphene, nanocomposite, conductivity, electron transport

I. Introduction

Graphene is a single layer of carbon atoms arranged in a honeycomb lattice. Single-layer graphene is a unique two dimensional material, of which the π-bands are responsible for charge carrier transport[1]. Since its discovery in 2004, numerous research has been carried on this kind of material. It has been proved to have superior electric conductivity, thermal conductivity and mechanical strength [2-5]. It has huge potential to be applied in solar cell[6] and display[7] as transparent electrodes, in high frequency transistor[8, 9] and highly sensitive sensor[10, 11] as functional materials. It also could be applied in composite materials as fillers [12, 13]. Polypyrrole (PPy) is an insulator, but its oxidized derivatives are good electrical conductors. After oxidization (doping), the double bonds of which could form transport path for charge carriers. Charge carriers transport on the backbone of polymer chain, and there is some crosslinking of polymer chains and charge carriers have to hop between the polymer chains, so it is described as "quasi unidirectional" vs. one-dimensional[14]. Since it will expand during charging and sensitive to humidity and some gas, it is widely used an artificial muscle and biochemical sensor [15-18]. Nanocomposite consists of graphene nanoplatelets and polypyrrole has been studied recently as well, which is reported to have potential to be used in supercapacitors [12, 19, 20].

Graphene could be obtained by many ways, such as CVD, reduced graphene oxide, direct exfoliation. Direct exfoliation is used in this study. The main reason is because its final product is dispersion, which could be mixed with pyrrole monomers directly. Pyrrole could be polymerized by chemical oxidization and electrochemical oxidization. Chemical oxidization is chosen in this study to get a liquid dispersion directly, and the oxidize agent is ammonia persulfate (APS). A nanocomposite consists of graphene nanoplatelets and polypyrrole using one step in-situ polymerization has been formed in this study. The effect of graphene concentration on conductivity has been investigated and reported. The electron transport mechanism of this nanocomposite has been studied.

II. Experimental

Pyrrole monomers were purchased from Alfa Aesar with purity of 98+%. Ammonia persulfate (ASP) was purchased from Sigma-Aldrich. Graphite was purchased from Alfa Aesar with size of -20+80 mesh and purity of 99.9%. Graphene was purchased from Cheap Tubes. Hydrochloride was purchased from Alfa Aesar. All chemicals were used as received.

Graphene dispersions with different concentration were prepared. In a beaker 3 g of graphite was mixed with 60 mL isopropanol, and the mixture was sonicated for 90 min. After setting the mixture aside for 1 hour, upper dispersion was collected, which is the original graphene dispersion. Graphene dispersion with higher concentration (three times of the original) was obtained by evaporating graphene

isopropanol at 60 °C in a petri dish to one third of its original volume and sonicated the resultant for 60 min. To get higher concentration of graphene, 0.05 g of purchased graphene powder was dispersed in 2 mL of isopropanol by sonication for 60 min.

In a beaker 2 mL of graphene dispersion was mixed with 0.03 M of pyrrole monomers, and the mixture was sonicated for 30 min. After sonication, it was put in ice bath for 10 min to pre-condition the mixture. One drop of HCl was added into the mixture while sonicating the mixture in ice bath, and 2 mL of pre-conditioned ammonia persulfate with concentration of 0.66 mM/mL was added in during sonication drop wisely. Reaction lasted for 3 hours, during which ice bath sonication was continued through. Resultant liquid mixture was centrifuged at 1500 rpm for 2 minutes. After centrifuge the liquid will be divided into two parts as shown in Fig. 1. Black polypyrrole-graphene ink floated on top, clear nonreacted pyrrole monomers were cumulated at bottom. By using a pipette, the ink on top was collected and put in a container in refrigerator. A control group is prepared by mixing polypyrrole fine powder with purchased graphene in isopropanol directly by sonicating for 60 min in order to verify the advantage of in-situ polymerization. Resultant inks with different composition were deposited on glass slides using a brush on hot plate. Glass slides were heated on a hot plate at 40 °C. The ink was deposited on glass slides layer by layer. Total five layers were deposited on each glass slide, with an average thickness of 0.003 mm.

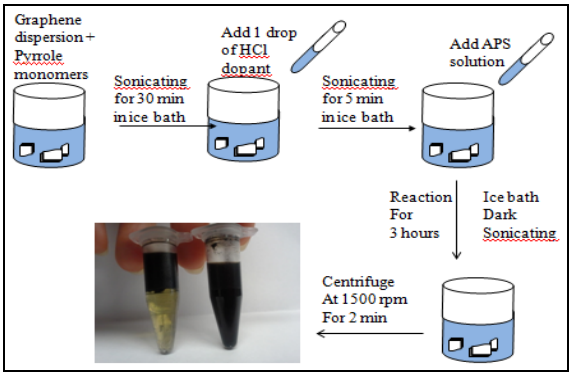

Figure 1 Illusion of synthesis procedure of polypyrrole/graphene ink

III. Results and Discussion

After deposition, in-situ polymerization samples were washed by methanol and deionized water and dried. XRD images were taken for samples of pure polypyrrole (PPy), polypyrrole with original graphene dispersion (PPy-Gr), polypyrrole with condensed graphene dispersion (PPy-3Gr), polypyrrole with purchased graphene nanoplatelets (PPy-B-Gr), and direct mixture of polypyrrole powder and purchased graphene nanoplatelets, the graphene concentration of each sample were listed in Table 1. From Fig. 2, the peak indicating graphene nanoplatelets at 26.6º is not strong for PPy-Gr, PPy-3Gr and PPy-B-Gr, while is pretty pronounced for DirectMix-PPy-B-Gr. Since the graphene concentration for the PPy-B-Gr is 10%, which is similar to the concentration of DirectMix-PPy-B-Gr (10%), this could be explained by that during polymerization, polypyrrole was formed a polymer layer surrounding graphene nanoplatelets.

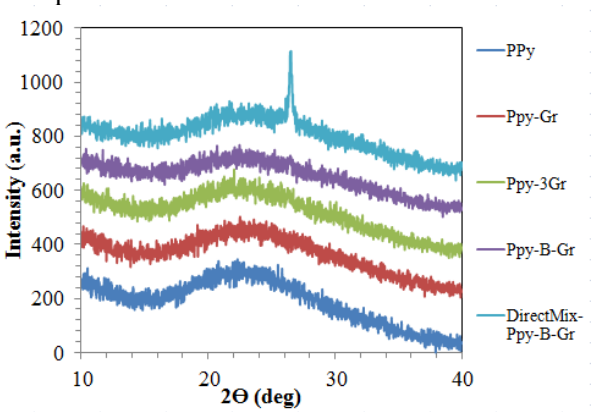

Figure 2 X-ray diffraction patterns of polypyrrole/graphene nanocomposites with different concentration of graphene

TABLE I CONDUCTIVITY OF FILM SAMPLES WITH DIFFERENT GRAPHENE CONCENTRATION

Sample	Conductivity (s/m) at 298 K	Graphene Concentration (wt%)
ppy	4.08	0
ppy-Gr	3.61	0.09%
ppy-3Gr	3.60	0.27%
ppy-B-Gr	1.61	10%
DirectMix-Ppy-B-Gr	-	10%

Conductivity of graphene/polypyrrole film was evaluated by two probe methods. Two parallel aluminum electrodes with rectangular shaped space between them were deposited on samples

by physical vapor deposition. Table 1 shows that as graphene concentration increase, the conductivity of nanocomposite decreased. That suggested the existence of graphene in polypyrrole didn't contribute to the charge carriers transport positively in the nanocomposite film. Conducting polymers could be seen as one-dimensional conducting chains, which have backbones of contiguous sp^2 hybridized carbon centers forming a conducting path. Disorder and one-dimensionality of polypyrrole lead to localization of the electron wave functions[14, 21]. Conductivity decrease in Table 1 suggested that during polymerization, graphene introduced more disorder and defects. That is supported by the surface morphology in Figure 3. With a much higher concentration of graphene, the PPy-B-Gr sample has a much rougher surface than pure PPy and PPy-3Gr.

The temperature dependence of conductivity of this nanocomposite was studied. Figure 4 shows the $\ln(\sigma)$ vs.T^{-1} curves of sample PPy, PPy-Gr and PPy-B-Gr. The temperature dependence of all the samples could be described by Arrhenius equation:

$$\sigma = \sigma_o \exp\left(\frac{E_a}{k_B T}\right)$$

where, σ is conductivity, σ_o is dependent on material, k_B is Boltzmann constant, T is temperature, and E_a could be seen as activation energy needed for the carrier to hop or diffuse from one polymer chain to another. From Figure 4, the negative coefficient shows semiconductor behavior of this nanocomposite. There is not much difference in the calculated activation energy for each sample, which indicates that the dominant electron transport mechanism is the same as polypyrrole, and the energy need by charge carriers to hop between polymer chains is not effected by graphene.

Figure 5 shows O_2 plasma treatment effect on surface conductivity. Trend of O_2 Plasma treatment reduced the activation energy is observable, however not very pronounced. That maybe due to oxidation during plasma treatment completed the undoped path in polymer chain.

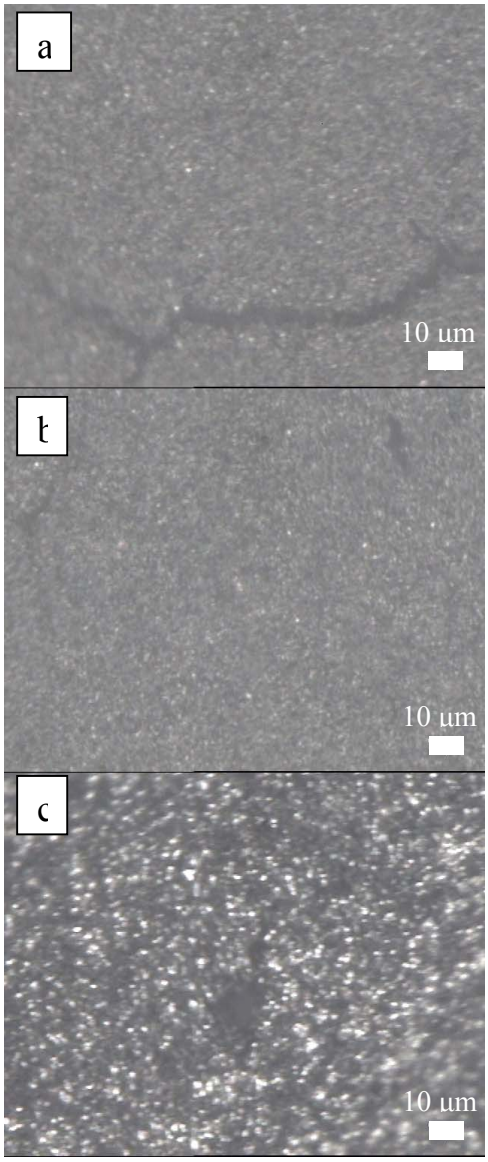

Figure 3 Optical microscopic images of sample (a) PPy, (b) PPy-3Gr, (c) PPy-B-Gr.

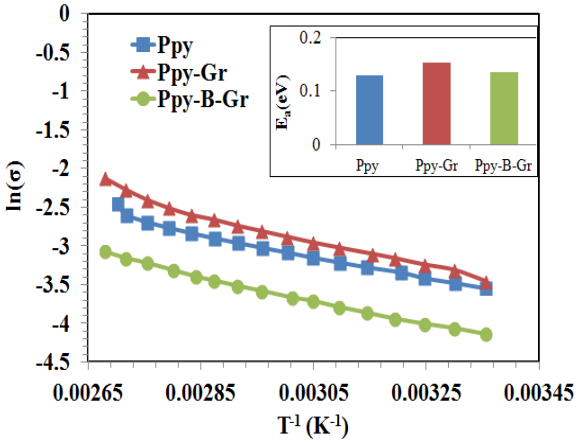

Figure 4 ln(σ) vs. T^{-1} curves for sample PPy, PPy-Gr and PPy-B-Gr.

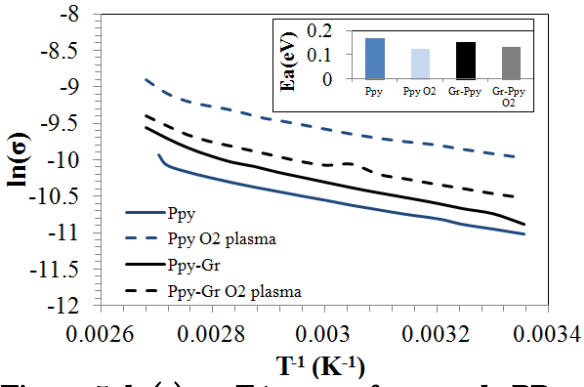

Figure 5 ln(σ) vs. T^{-1} curves for sample PPy, PPy with O_2 plasma treatment, PPy-Gr, and PPy-Gr with O_2 plasma treatment.

IV. Conclusion

A synthesis method of graphene/polypyrrole nanocomposite ink was demonstrated. Since both polypyrrole and graphene are not soluble and fusible, compare to direct mix solution, in-situ polymerization ink could produce a film with better integrity, and the ink could be deposited as conventional ink. Conductivity of polypyrrole/graphene nanocomposite film formed by this ink has been studied. Compare to polypyrrole, graphene contributes to conductivity negatively. O_2 plasma treatment is found to increase the conductivity and reduced the activation energy a little bit. Temperature dependence of conductivity was studied, and the dominant electron transport mechanism of nanocomposite is the same as PPy, and not effected by graphene fillers.

Reference

[1] Novoselov KS, Geim AK, Morozov SV, Jiang D, Katsnelson MI, Grigorieva IV, et al. Two-dimensional gas of massless Dirac fermions in graphene. Nature. 2005;438:197-200.

[2] Balandin AA, Ghosh S, Bao W, Calizo I, Teweldebrhan D, Miao F, et al. Superior Thermal Conductivity of Single-Layer Graphene. Nano letters. 2008;8:902-7.

[3] Das Sarma S, Adam S, Hwang EH, Rossi E. Electronic transport in two-dimensional graphene. Reviews of Modern Physics. 2011;83:407-70.

[4] Du X, Skachko I, Barker A, Andrei EY. Approaching ballistic transport in suspended graphene. Nature nanotechnology. 2008;3:491-5.

[5] Lee C, Wei X, Kysar JW, Hone J. Measurement of the elastic properties and intrinsic strength of monolayer graphene. Science. 2008;321:385-8.

[6] Zhang DW, Li XD, Li HB, Chen S, Sun Z, Yin XJ, et al. Graphene-based counter electrode for dye-sensitized solar cells. Carbon. 2011;49:5382-8.

[7] Bae S, Kim H, Lee Y, Xu X, Park JS, Zheng Y, et al. Roll-to-roll production of 30-inch graphene films for transparent electrodes. Nature nanotechnology. 2010;5:574-8.

[8] Dimitrakopoulos C, Lin Y-M, Grill A, Farmer DB, Freitag M, Sun Y, et al. Wafer-scale epitaxial graphene growth on the Si-face of hexagonal SiC (0001) for high frequency transistors. Journal of Vacuum Science & Technology B: Microelectronics and Nanometer Structures. 2010;28:985.

[9] Lee Y, Bae S, Jang H, Jang S, Zhu SE, Sim SH, et al. Wafer-scale synthesis and transfer of graphene films. Nano letters. 2010;10:490-3.

[10] Arsat R, Breedon M, Shafiei M, Spizziri PG, Gilje S, Kaner RB, et al. Graphene-like nano-sheets for surface acoustic wave gas sensor applications. Chemical Physics Letters. 2009;467:344-7.

[11] Zhao J, Zhang G-Y, Shi D-X. Review of graphene-based strain sensors. Chinese Physics B. 2013;22:057701.

[12] Bose S, Kim NH, Kuila T, Lau K-t, Lee JH. Electrochemical performance of a graphene-polypyrrole nanocomposite as a supercapacitor electrode. Nanotechnology. 2011;22:369502.

[13] Ramanathan T, Abdala AA, Stankovich S, Dikin DA, Herrera-Alonso M, Piner RD, et al. Functionalized graphene sheets for polymer nanocomposites. Nature nanotechnology. 2008;3:327–31.

[14] Kohlman RS, Epstein AJ. Insulator-matal transition and inhomogeneous metallic state in conducting polymers. Handbook of conducting polymers. 1998;3:85-119.

[15] Ateh DD, Navsaria HA, Vadgama P. Polypyrrole-based conducting polymers and interactions with biological tissues. Journal of the Royal Society, Interface / the Royal Society. 2006;3:741-52.

[16] Hernandez SC, Chaudhuri D, Chen W, Myung NV, Mulchandani A. Single Polypyrrole Nanowire Ammonia Gas Sensor. Electroanalysis. 2007;19:2125-30.

[17] Ramanavičius A, Ramanavičienė A, Malinauskas A. Electrochemical sensors based on conducting

polymer—polypyrrole. Electrochimica Acta. 2006;51:6025-37.
[18] Kim H, Kwon S. Materials science. Water-responsive polymer composites on the move. Science. 2013;339:150-1.
[19] de Oliveira HP, Sydlik SA, Swager TM. Supercapacitors from Free-Standing Polypyrrole/Graphene Nanocomposites. The Journal of Physical Chemistry C. 2013;117:10270-6.
[20] Xu C, Sun J, Gao L. Synthesis of novel hierarchical graphene/polypyrrole nanosheet composites and their superior electrochemical performance. Journal of Materials Chemistry. 2011;21:11253.
[21] Cheah a K, Forsyth a M, Truong b V-T. Ordering and stability in conducting polypyrrole. Synthetic Metals. 1998;94:215-9.

Experimental Study on Thin Film Cu_2ZnSnS_4 Deposition by Spin Coating

Mahdi Rajabpour, Zhengqi Shi and Ahalapitiya H. Jayatissa[a]

Nanotechnology and MEMS Laboratory, Department of Mechanical, Industrial and Manufacturing Engineering (MIME), University of Toledo, Ohio, USA
[a]Ahalapitiya.Jayatissa@UToledo.edu

ABSTRACT

This paper reports a simple approach to synthesis Cu_2ZnSnS_4 (CZTS) thin film over the glass substrate by spin coating. A precursor solution of inorganic salts of Cu (II) and Zn (II) and Sn(II) along with thiourea in methanol was prepared at room temperature. Drying of deposited layers was carried out through two different procedures followed by an annealing at 500°C temperature for 2 h in N_2. The X-Ray Diffraction (XRD) results confirmed partially formation of CZTS crystal, while there was still considerable amount of oxides inclusions in the films. However, oxidation largely reduced by drying films in N_2.

Keywords: CZTS, Thin film coating, solar cell

I. INTRODUCTION

There is a growing research interest in synthesis of Cu_2ZnSnS_4 (CZTS) as a serious alternative of CIGS for next generation of solar cells. Containing only nontoxic earth abundant elements, CZTS is a P-type semiconductor with kesterite crystal structure and desired electrical and optical properties (tunable band gap energy and optical absorption coefficient), which all together introduce it theoretically as quite ideal material for absorber layer in a solar unit.[1-3]

Considering this promising prospective, several efforts have been done to synthesis CZTS(Se) in form of powder or deposited layer. Different methods have already proposed for CZTS production, including vacuum based approach (Sputtering, thermal evaporation) and Non-vacuum approach (mainly solution based methods).[4-6] Regarding drawbacks in vacuum based techniques (expensive, need for high vacuum and complicated apparatus) there is a common intention towards developing facile, inexpensive and robust non vacuum methods to synthesis CZTS material.[6]

Following solution-based approach, several research groups could successfully synthesis and employ CZTS(Se) powder/film to fabricate a solar cell device. Sun et all[7] have dip-coated CZTSSe thin film over Glass substrate using fully dissolved CZTS precursor solution. Preparing solution of thioacetamide and salt chlorides of Cu(I), Zn(II), Sn(IV) in a proper solvent (Ethanol and Monoethanolamine (MEA)), film layers deposited and annealed at 480oC for 30 min under Se vapor. A solar unit device with such a synthesized material as absorber layer has shown efficiency of 5.36% . Guo et al[8] have implemented hot-injection method along with knife coating to achieve densely packed CZTSSe thin film. Taking cupper-poor/zinc- rich approach, salt (acetylacetonate) solution of Cu(II), Zn(II) and Sn(IV) in Oleyamine (solvent) heated gently at 130°C for 30 min under Ar purge. Increasing reaction temperature to 225°C, solution of S-Oleyamin injected to the flask and heated for 30 min. Resulted nanoparticle crystals used for knife coating over glass substrate and then annealed at 500°C for 20 min in Se vapor. They have reported an efficiency of 7.2% for a solar cell unit using this absorber layer. In an another attempt, Schnabel et al[9] have adopted blade coating method to make CZTSSe absorber layer for a solar cell with cell efficiency of 7.5%. Precursor mixture prepared via dissolving metal salts and thiourea in solvent (dymethyle solfuxid) at room temperature. Deposited film dried in N_2 at 300°C for 1 min, followed by final annealing in Se atmosphere at 540°C for 6 min. Among all reported CZTS(Se) based fabricated solar cell, a vacuum-free hydrazine solution based synthesized CZTSSe, developed by IBM, achieved highest record efficiency of 11.1%. Making a proper precursor solution of Cu(I), Zn(II), Sn(II) in hydrazine, thin film spin coated over the substrate, followed by annealing on hot plate (at 540°C) under S atmosphere.[10]

Some other groups mainly concentrated over synthesis and characterization of CZTS(Se) powders and nanoparticles through solution based methods. As a simple inexpensive synthesis technique using non toxic solvent, Hydrothermal route has recently considered a potential method to make CZTS(Se) powder.

Wang et al[11] have reported hydrothermal synthesis of CZTS nano crystal powder with band gap of 1.7 eV. Reaction precursor, mixture of salt chlorides of Cu(I), Zn and Sn(IV) and Thiourea (concentration ratio 2:1:1:4) in DI water, heated in different reaction conditions (time-temperature)

inside an autoclave, with best results achieved at 200°C for 30 h. Using similar salts and thiourea with concentration ratio of (2:1:1:12), Hsu et al[12] have claimed to obtain pure CZTS powder, with band gap of 1.45 eV, by heating rich sulfur precursor at 180°C for 72 h inside an autoclave. Kush et al[13] have employed Na_2S as sulfur source for DI water based precursor with chloride salts of Cu(II), Zn(II) and Sn(II) and concentration ratio of 2:1:1:4. Reaction completed via heating precursor solution at 180°C for 18 h, resulted in formation of CZTS nano crystal powder (aggregated particles) with band gap energy 1.75 eV. In another attempt similar to Kush[13] studies, Liu et al[14] have dissolved stochiometric ratio of Cu(II), Zn(II) and Sn(II) elements (using chloride salt and other proper salts) and Thiourea in a solution of DI water and Ethylenediamine (stabilizer and chelating agent). Heating precursor at 180°C for 24 h, CZTS nano crystal particles with band gap energy of 1.47 eV have claimed to be achieved. In a similar research work by this group, it is shown that increasing reaction time from 6 h to 48 h, the final CZTS particle size will increase from 3 nm to 10.5 nm. [15]

Here we report a simple approach to spin coat a CZTS thin film on the glass substrate using a precursor mixture of metal salts and chalchogenide in methanol. Coated samples was dried in the same temperature but different atmosphere and then annealed at 500°C for 2 h in N_2. A conclusion over XRD result was finally provided.

II. EXPERIMENTAL DETAILS

To prepare precursor solution, 5 mmol of cupric(II)Nitrate ($Cu(No_3)_2.2.5H_2O$ Fisher Scientific), 2.5 mmol of Zinc(II)Nitrate.Hegzahydrate ($Zn(No_3)_2.6H_2O$ Fisher Scientific), 2.5 mmol of Tin(II)-ethylhexanoate (SIGMA 95%), 10 mmol of thiourea (CH_2SNH_2, Fisher Scientific) and 80 ml of Methanol (purity 98%) were chosen. Dissolving metal salts and thiourea in methanol (20 mmol) in separate beakers, metal salt solutions mixed together and stirred for 20 min to obtain a clear blue-green solution. In next step, thiourea solution added to the current metals solution, the mixture stirred for 15 min. Following addition of thiourea, white gel colloidal precipitated in remaining transparent colorless solvent. The obtained precursor employed to spin coated over two samples (precisely cleaned glass substrates (1x1 cm^2)) with different drying procedures.

For the first sample, proper amount of mixture were dropped on the substrate and film layer deposited through spin coating at 500 RPM for 20 s, followed by intermittent drying over hot plate substrate at 230°C for 3 min. Over drying, color of deposited layer changes from white to dark black. Repeating this procedure for 20 times, a thin film deposited over the substrate.

For the sample two, deposition procedure was the same as first sample, except for drying stage, where in the second sample each deposited layer dried at room temperature in air without heating. Final coated sample was then dried at 230°C for 1 h in N_2.

To improve film crystal structure, both samples were annealed at 500°C for 2 h in N_2 flow, and then cooled down to room temperature very slowly.

III. RESULTS AND DISCUSSIONS

X-Ray diffractometer (PANalytical X'Pert Pro MPD), with Cu Kα radiation was employed to measure XRD patterns of both coated samples. Regarding XRD results, first sample was seemed to be a combination of SnO_2 (score 80), ZnS (score 54) and CZTS (score 27) (Fig. 1), while the second sample mainly consisted of SnO_2 (score 85) and CZTS (score 72) (Fig. 2). Moreover, main peak in sample one belonged to SnO_2, while CZTS represented the main peak in sample two, which verified formation of higher amount of CZTS in second sample. These results indicated that synthesis of CZTS in sample two was more successful than sample one, which mainly could be attributed to applying different drying stage. In sample one, each deposited layer was dried in air at relatively high temperature, leading to oxidation of Sn elements of precursor, while in sample two, N_2 atmosphere to somehow prevented precursor from oxidation. Therefore more oxides were expected to present in final layer in sample one than sample two. In addition, annealing the samples in high temperature was another probable source of oxidation. Despite using ultra high purity N_2 as protection atmosphere in annealing, very few amount of oxygen could be still available in the atmosphere, probably high enough to oxidize part of film in high temperature during annealing.

However, as XRD pattern of CZTS crystal is similar to some binary compounds like ZnS, Cu_2SnS_4 and Cu_2S, further examination like Raman Spectroscopy is required to precisely identify crystal structure of coated film.

IV.CONCLUSION

Synthesis and coating of CZTS thin film was studied in this paper. Using XRD pattern of crystal structures, two different films were compared from synthesis point of view. It was revealed that oxidation prevention is a crucial stage in making film, both in film drying and annealing stages. Moreover it was shown that more synthesis tuning was needed to reach pure CZTS film

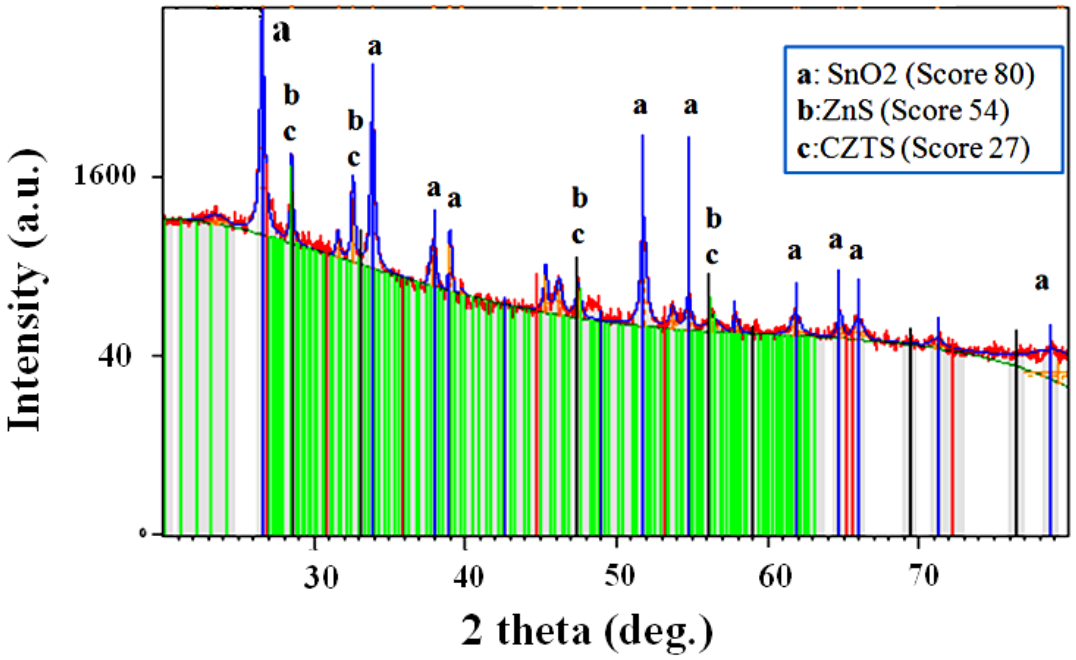

Fig. 1: XRD pattern of CZTS film dried (each layer) at 230°C for 3 min on hot plate in air (Sample one).

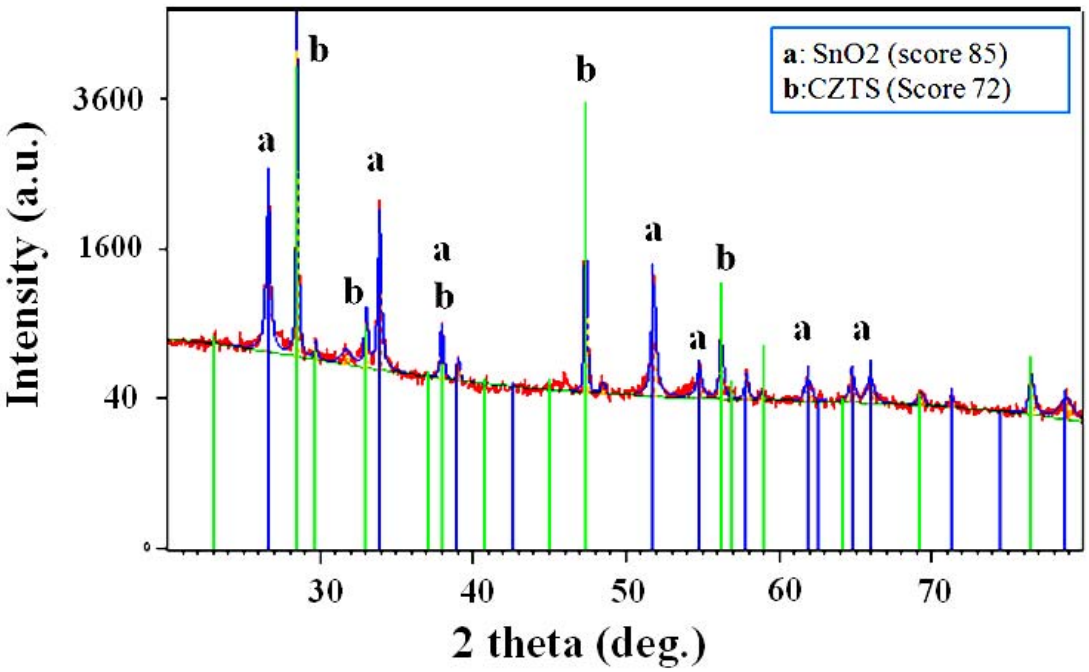

Fig. 2: XRD pattern of CZTS film dried at 230 °C for 1 h in N_2 (sample two).

V.Acknowledgment: University of Toledo primarily supports the conference (Grant No. ECS-0928440).

VI.REFERENCES

[1] Mitzi DB, Gunawan O, Todorov TK, Wang K, Guha S. The path towards a high-performance solution-processed kesterite solar cell, Solar Energy Materials & Solar Cells 95(2011) 1421-1436.

[2] Kumar YB, Suresh Babu G, Uday Bhaskar P, Sundara Raja V. Preparation and characterization of spray-deposited Cu_2ZnSnS_4 films, Solar Energy Materials and Solar Cells 93 (2009) 1230.

[3] Redinger A, Berg DM, Dale PJ, Djemour R, Gütay L, Eisenbarth T, Valle N, Siebentritt S. Route towards high-efficiency single-phase $Cu_2ZnSn(S,Se)_4$ thinfilm solar cells: model experiments and literature review; IEEE Journal of Photovoltaics 1 (2011) 200.

[4] Siebentritt S, Schorr S. Kesterites a challenging material for solar cells, Prog. Photovolt Res. Appl. 2012; 20:512–519.

[5] Delbos S. Kesterite thin films for photovoltaics: a review, EPJ Photovoltaics 3, 35004 (2012).

[6] Abermann S. Non-vacuum processed next generation thin film photovoltaics: Towards marketable efficiency and production of CZTS based solar cells, Solar Energy 94 (2013) 37–70.

[7] Sun Y, Zhang Y, Wang H, Xie M, Zong K, Zheng H, Shu Y, Liu J, Yan H. Novel non-hydrazine solution processing of earth abundant $Cu_2ZnSn(SSe)_4$ absorbers for thin film solar cells, J. Mater. Chem. A, 2013,1,6880.

[8] Guo Q, Ford GM, Yang WC, Walker BC, Stach EA, Hillhouse HW, Agrawal R. Fabrication of 7.2% Efficient CZTSSe Solar Cells Using CZTS Nanocrystals, J. AM. CHEM. SOC. 2010, 132, 7384–17386.

[9] Schnabel T, Löw M, Ahlswede E. Vacuum-free preparation of 7.5% efficient $Cu_2ZnSn(S,Se)_4$ solar cells based on metal salt precursors, Solar Energy Materials & Solar Cells 117 (2013) 324–328.

[10] Todorov TK, Tang J, Bag S, Gunawan O, Gokmen T, Zhu Y, Mitzi DB, Beyond 11% fficiency characteristics of state-of-the-art Cu2ZnSn(S,Se)4 solar cells; Advanced Energy Materials 3, 2013, 34.

[11] Wang C, Cheng C., Cao Y, Fang W, Zhao L, Xu X. Synthesis of Cu_2ZnSnS_4 Nanocrystallines by a Hydrothermal Route, Japanese Journal of Applied Physics 50 (2011) 065003.

[12] Hsu KC, Liao JD, Chao LM, Fu YS. Fabrication and Characterization of Cu_2ZnSnS_4 Powders by a Hydrothermal Method, Japanese Journal of Applied Physics 52 (2013) 061202.

[13] Kush P, Ujjain SK, Mehra NC, Jha P, Sharma RK, Deka S. Development and Properties of Surfactant-Free Water- Dispersible Cu_2ZnSnS_4 Nanocrystals: A Material for Low- Cost Photovoltaics; ChemPhysChem 2013, 14, 2793 – 2799.

[14] Liu W, Guo B, Mak C, Li A, Wu X, Zhang F. Facile synthesis of ultrafine Cu_2ZnSnS_4 nanocrystals by hydrothermal method for use in solar cells, Thin Solid Films 535 (2013) 39–43.

[15] Liu WC, Guo BL, Wu XS, Zhang FM, Mak CL, Wong KH. Facile hydrothermal synthesis of hydrotropic Cu_2ZnSnS_4 nanocrystal quantum dots: band-gap engineering and phonon confinement effect, J. Mater. Chem. A, 2013, 1, 3182–3186.